

## Getting the electrons right for O2-on-metal systems Bree, R.A.B. van

#### Citation

Bree, R. A. B. van. (2025, October 21). *Getting the electrons right for O2-on-metal systems*. Retrieved from https://hdl.handle.net/1887/4279459

Version: Publisher's Version

Licence agreement concerning inclusion of doctoral

License: thesis in the Institutional Repository of the University of

<u>Leiden</u>

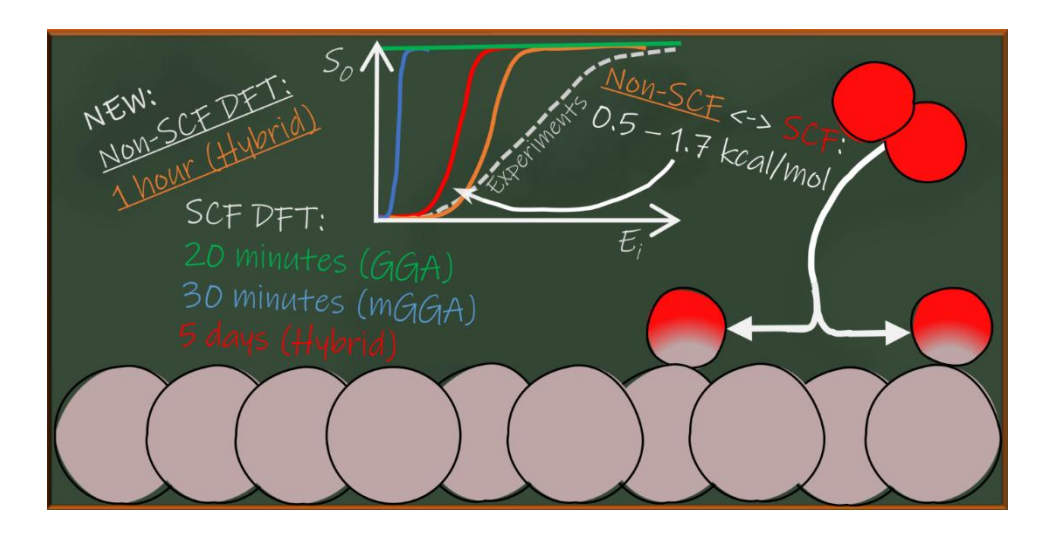
Downloaded from: <a href="https://hdl.handle.net/1887/4279459">https://hdl.handle.net/1887/4279459</a>

**Note:** To cite this publication please use the final published version (if applicable).

3 Dissociative chemisorption of O<sub>2</sub> on Al(111): Dynamics on a potential energy surface computed with a non-self-consistent screened hybrid density functional approach

#### This chapter is based on:

van Bree, R. A. B.; Gerrits, N.; Kroes, G.-J. Dissociative Chemisorption of  $O_2$  on Al(111): Dynamics on a Potential Energy Surface Computed with a Non-Self-Consistent Screened Hybrid Density Functional Approach. *Faraday Discuss.* **2024**, *251*, 361–381. https://doi.org/10.1039/D3FD00165B.



## Abstract

Density functional theory (DFT) at the generalised gradient approximation (GGA) level is often considered the best compromise between feasibility and accuracy for reactions of molecules on metal surfaces. Recent work, however, strongly suggests that density functionals (DFs) based on GGA exchange are not able to describe molecule-metal surface reactions for which the work function of the metal surface minus the electron affinity of the molecule is less than 7 eV. Systems for which this is true exhibit an increased charge transfer from the metal

to the molecule at the transition state, increasing the delocalisation of the electron density. This enlarged delocalisation can cause GGA-DFT to underestimate energy values relative to the gas-phase and thus underestimate the barrier height, similar to what has been observed for several gas-phase reactions. An example of such a molecule-metal surface system is  $O_2 + Al(111)$ . Following a similar strategy as for gas-phase reactions, previous work showed results of increased accuracy when using a screened hybrid DF for  $O_2 + Al(111)$ . However, even screened hybrid DFs are computationally expensive to use for metal surfaces. To resolve this, we test a non-self-consistent field (NSCF) screened hybrid DF approach. This approach computes screened hybrid DFT energies based on self-consistent-field (SCF) GGA electronic densities. In this chapter, we explore the accuracy of the NSCF screened hybrid DF approach by implementing the NSCF HSE03-1/3x@RPBE DF for O<sub>2</sub> + Al(111). We compute and analyse molecular beam sticking probabilities as well as a set of sticking probabilities for rotationally aligned O2. Our results show that the NSCF approach results in reaction probability curves that reproduce SCF results with near-chemical accuracy, suggesting that the NSCF approach can be used advantageously for exploratory purposes. An analysis of the potential energy surface and the barriers gives insight into the cause of the disagreement between the SCF and NSCF reaction probabilities and into the changes needed in theoretical modelling to further improve the description of the  $O_2$  + Al(111) system. Finally, the hole model yields fair agreement with dynamics results for the reaction probability curve, but results in an increased slope of the reaction probability curve compared to the molecular dynamics, with a shift to lower or higher energies depending on whether the vibrational energy of the molecule is included in the initial energy of the molecule or not.

#### 3.1 Introduction

The dissociative chemisorption (DC) of a molecule reacting on a surface is often rate-controlling step in heterogeneously catalysed processes<sup>6,212,213</sup>, for instance in ammonia production<sup>1,5</sup>, and steam reforming<sup>27,28</sup>. Moreover, the DC of an O<sub>2</sub> molecule is the initial and often the rate-determining step in oxide formation, corrosion, and catalytic oxidation reactions<sup>214–218</sup>. Understanding the elemental steps at play in the DC of O<sub>2</sub>, or other diatomic molecules, is thus of great practical importance. In addition, there is also an intrinsic scientific interest in understanding the breaking and formation of chemical bonds at surfaces<sup>1,55,56,219,220</sup>. In the literature, the H<sub>2</sub> on Cu(111) system is often mentioned as the benchmark system for H<sub>2</sub> dissociation<sup>55,110,135,221</sup>. Similarly, O<sub>2</sub> on Al has over the years become the benchmark system for the oxidation of metals<sup>214,222–227</sup>. However, theoretical work on the DC of O<sub>2</sub> on Al(111) has thus far not been able to come to an overall consensus on the barrier height for dissociation, the origin of the barrier, and even the reaction mechanism at play<sup>228–235</sup>.

The foremost reason for the disagreement in the theoretical community is that density functionals (DFs) at the generalised gradient approximation (GGA) level of density functional theory (DFT) fail to yield even a qualitatively correct description of the O<sub>2</sub> + Al(111) reaction. The workhorse GGA DF for modelling gas metal interactions<sup>56</sup>, the PBE<sup>154</sup> DF, fails to predict any barriers for DC of O<sub>2</sub> on Al(111)<sup>236–238</sup>. Moreover, even one of the most repulsive (and therefore 'least reactive') DFs that can be used for molecule-metal systems at the GGA DFT level, the RPBE functional<sup>239</sup>, fails to predict any significant barrier for the dissociation of O<sub>2</sub> on Al(111)<sup>236–238</sup>. GGA-level functionals generally incorrectly predict unit reaction probabilities for all incidence energies, i.e., GGA DFs predict a nonactivated reaction<sup>124</sup>. This is in contrast with experimental evidence, which shows that the DC of O<sub>2</sub> on Al(111) is an activated reaction<sup>224</sup>. Going beyond semi-local (GGA) functionals to resolve this (or for gas-metal systems in general) is still challenging as computational costs increase quickly and the dual nature of the system, i.e. the presence of both molecule and metal surface, makes the choice of functional more difficult. As such, a solution to the theoretical description of the O<sub>2</sub> on Al(111) system is not readily found.

The failure of GGA-DFT to describe the barrier of O<sub>2</sub> dissociation on Al(111) has, over the years, been attributed to different origins. Behler et al. 231,240 argued that the reaction should proceed in an almost diabatic fashion, with spin-orbit coupling only being strong enough to quench the triplet spin of the oncoming O<sub>2</sub> molecule once the barrier on the corresponding 'triplet potential energy surface' has already been passed. They argued that in GGA or other adiabatic DFT approaches, this quenching (which is forbidden in the absence of spin-orbit coupling) incorrectly happens continuously, already occurring for O<sub>2</sub> still far from the surface. This should then be why the sticking probability should be overestimated at the adiabatic RPBE-GGA level of theory, as found in Ref. <sup>231</sup>. Using an RPBE-DFT approach for computing the potential energy surface (PES) in which the spin state on O<sub>2</sub> was locally constrained to the triplet ground state, they obtained semi-quantitative agreement with sticking experiments in classical molecular dynamics (MD) calculations<sup>231,240</sup>. Carbogno et al.<sup>234,235</sup> later made predictions for experiments on the scattering of singlet O<sub>2</sub> from Al(111) that can be used to verify the proposed mechanism, but these experiments have not yet been carried out.

Later, Carter and co-workers argued that the barrier for dissociation of O2 on Al(111) does not find its origin in spin selection rules but in the occurrence of charge transfer<sup>228</sup>. As Carter and co-workers showed, they were able to compute rather accurate DC barriers for O<sub>2</sub> + Al(111) using an adiabatic approach<sup>228–230</sup> employing an embedded correlated wavefunction (ECW) method<sup>241</sup>. In these calculations, a second-order multi-reference perturbation theory method, i.e., CASPT2<sup>242,243</sup>, was used to model the interaction of O<sub>2</sub> with an embedded Al cluster. Carter and co-workers attributed<sup>228</sup> the errors in approaches based on GGA DFs to the lack of derivative discontinuities<sup>244</sup> and the self-interaction error<sup>245</sup>. Dynamics calculations based on an embedded CASPT2 PES were in semi-quantitative agreement with sticking experiments<sup>230</sup>, thereby showing that modelling non-adiabatic effects associated with spin-orbit coupling may not be necessary. A disadvantage of their method is that CASPT2 calculations are rather expensive computationally, with the cost scaling as  $O(N^5)$  where N is a measure of the size of the system<sup>246</sup>. Perhaps due to high computational costs, the PES was fitted using a minimum of data points, and as a result, a fitting method with limited accuracy (the flexible periodic London-Eyring-Polanyi-Sato,

FPLEPS<sup>210,247,248</sup> method) had to be used. Furthermore, this unfavourable scaling has possibly stood in the way of achieving further progress using this method for molecules interacting with transition metal surfaces<sup>116,129</sup>, though recent calculations on  $H_2$  + Cu(111) show much better results with the embedded NEVPT2 method<sup>249</sup>.

One method to correct for the self-interaction error, at least approximately, is to mix exact non-local exchange with semi-local exchange to obtain a hybrid DF This approach has been used successfully to obtain DFs that are more accurate for gas-phase reaction barriers<sup>137,139</sup>. This idea was further supported by preliminary hybrid DFT calculations on  $O_2 + Al(111)$ , showing that barriers for dissociation do occur when employing (screened) hybrid functionals to calculate the electronic structure<sup>226</sup>. The suggestion to go beyond the use of semi-local functionals for  $O_2 + Al(111)$  also comes from recent work suggesting a correlation between the failure of GGA-DFs for DC on metal surfaces with the so-called charge transfer energy of the system ( $E_{CT}$ ). This energy may be defined as:<sup>124</sup>

$$E_{CT} = \phi - EA \tag{3.1}.$$

Here,  $\phi$  is the work function of the metal surface, and *EA* is the electron affinity of the molecule. Gerrits *et al.* estimated<sup>124</sup> that the divide between GGA DF failure and success can be found at about  $7\,eV$ , i.e., if the charge transfer energy of a system is below  $7\,eV$ , charge transfer from metal to the molecule is more likely and an error in the semi-local GGA-DF is expected to occur and lead to underestimated barrier heights<sup>124</sup>. At  $3.76\,eV$  the charge transfer energy of the  $O_2$  on Al(111) system is far below  $7\,eV^{124}$ , and from previous work<sup>236,237</sup>, it is clear that a manner of delocalization of the  $O_2$  orbitals occurs at the Al surface, which has been pointed to as a cause for underestimating the barrier heights<sup>146,250,251</sup>. However, we do note that the work of Ref. <sup>124</sup> suggests that errors in the density are not necessarily the major cause of the underestimation of the barrier heights, as will be discussed further below.

The above-described correlation of the charge transfer energy of the system with the likely success of GGA functionals, the above-mentioned 'fix' for gasphase reactions, and preliminary results for  $O_2$  interacting with Al clusters<sup>230</sup> led to dynamics calculations using a screened hybrid DFT PES for  $O_2$  + Al(111)<sup>124</sup>. Hybrid DFT has a more favourable computational scaling with system size (as

 $O(N^4))^{252}$  than CASPT2. A screened hybrid functional was used as global hybrid DFs have severe shortcomings for metals, e.g., their use leads to an underestimated density of states at the Fermi level<sup>158</sup>. The screened hybrid functional dynamics calculations achieved semi-quantitative agreement with experimental sticking coefficients for  $O_2 + Al(111)^{124}$ .

The presented solution in Ref. 124 is promising, nevertheless, the use of screened hybrid functionals for gas-metal systems (even for simple metals like AI) is computationally expensive. Nonetheless, if the error of the GGA functional would be mostly functional-driven<sup>253</sup> as opposed to density-driven<sup>124,253</sup>, the electron densities (and Kohn-Sham wavefunction) found from converged GGA DFT calculations might remain accurate. Consequently, using the GGA-DF electron density (and Kohn-Sham wavefunction) to non-self-consistently compute the energy with a screened hybrid functional might represent a viable (i.e., affordable) approach to systems with low electron transfer energies like O<sub>2</sub> + Al(111). This would enable us to avoid the majority of the computationally expensive cycles with the screened hybrid functional that would be required for self-consistency, and instead achieve results of (near) screened hybrid-level accuracy at only a fraction of the costs. Ref. 124 already suggested that this approach might be viable, by showing, for a limited number of configurations, that a non-self-consistent field (NSCF) hybrid calculation can indeed closely reproduce the self-consistent hybrid barrier heights 124,145 This finding suggests that the GGA error in the barrier heights for O<sub>2</sub> + Al(111) must be largely functional driven.

In this chapter, we explore the potential of the NSCF-screened hybrid functional approach by constructing and analysing an NSCF screened hybrid potential energy surface (PES) for  $O_2$  on Al(111) and using it in dynamics calculations. The resulting NSCF sticking probabilities are compared with SCF results and with results of supersonic beam experiments on sticking of ordinary and rotationally aligned beams. We will show that the NSCF approach reproduces SCF results to within  $2 \, kcal/mol$ . The NSCF results are unintentionally in even better agreement with experiments than the SCF results. Furthermore, an analysis of the PES and the reaction barriers, and an analysis using the hole model of Holloway and Nørskov and co-workers<sup>254</sup> give insight into the cause of the disagreement

between SCF and NSCF reaction probabilities. Our analysis also shows what type of additions in the theoretical modelling of this challenging benchmark system may be required in future work to improve upon the agreement presently achieved for  $O_2 + Al(111)$ .

This chapter is set up as follows. The next section, i.e., 3.2, presents the methods employed. Thereafter Section 3.3 presents the results in several sub-sections. The first sub-section, 3.3.1, discusses the importance of a strict convergence of the self-consistent calculations producing the GGA densities. The next two sub-sections, i.e., 3.3.2 and 3.3.3, present and discuss the results of the dynamics calculations using the NSCF PES for sticking of ordinary and rotationally aligned  $O_2$  in supersonic beams, also comparing to SCF and experimental results. After this, we discuss the role of the energetic corrugation of the barrier height in Section 3.3.4. Finally, Section 3.3.5 discusses results for  $O_2$  + Al(111) that are obtained with the hole model. After this the chapter is summarised in Section 3.4 and Section 3.5 presents two appendices.

#### 3.2 Methods

This section of Chapter 3 discusses the methods and computational details used for this work. This section is divided into six subsections. Section 3.2.1 discusses the coordinate system and dynamical model used, Section 3.2.2 the details of both DFs in use, Section 3.2.3 briefly highlights the computational details of the DFT calculations, 3.2.4 discusses the procedure for constructing the PES, 3.2.5 the relevant details for the QCT calculations, and lastly Section 3.2.6 discusses the computational implementation of the hole model.

## 3.2.1 Coordinate system and dynamical model

The coordinate system used in this chapter is as used in previous work on diatomic molecules reacting on (111) surfaces of FCC metals, see Ref. <sup>55</sup> for a detailed account. For the dynamics calculations in this chapter, we make use of the Born-Oppenheimer static surface (BOSS) approximation, which means that we employ both the Born-Oppenheimer approximation (BOA) and keep all Al(111) surface atoms fixed in their ideal lattice position<sup>56</sup>. This way, we only have

to consider the six degrees of freedom associated with the diatomic molecule  $(O_2)$ . Therefore, we can use the molecule's centre-of-mass (COM) centralised coordinate system for the molecule's degrees of freedom. In this coordinate system, the COM's position is expressed in the coordinates X and Y for motion along the surface, and Z is the distance of the molecule's COM to the surface. The distance between the oxygen atoms is given by the r coordinate. The azimuthal angle  $\varphi$  defines the orientation of the molecule's projection on the surface, i.e., on the horizontal-(X, Y)-plane, and the polar angle  $\theta$  defines the angle of the  $O_2$  bond axis with the Z-axis. For a visual representation see **Figure 3.1A**.

The surface unit cell of a (111) surface of an FCC metal is illustrated in **Figure 3.1B**. In this figure, the most relevant high-symmetry sites are also indicated. Note that the angle between the U and V axes can be taken as either 60 or 120 degrees; in **Figure 3.1B** the  $60^{\circ}$  version is demonstrated. As we are describing a unit cell, the U and V coordinates within this cell are taken as normalised (between 0 and 1). The X and Y coordinates of the COM of  $O_2$  are transformed to U, V-space to properly describe the position of the COM of  $O_2$  above a (111) FCC surface and its high symmetry sites, with the X vector being along U.

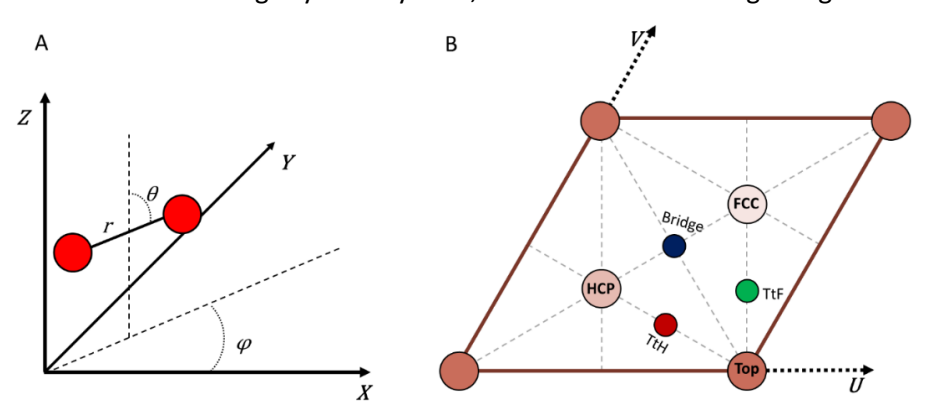


**Figure 3.1**: The coordinate system in use and its relation with the Al(111) surface unit cell. **A**: The centre-of-mass coordinate system used for the description of  $O_2$  interacting with Al(111). See the text for an explanation of the coordinates shown. **B**: The unit cell of a (111) surface of an FCC metal (Al), in which the high symmetry surface sites are indicated.

#### 3.2.2 Density functionals

The density functionals used for this chapter are the RPBE<sup>239</sup> DF at the generalised gradient approximation (GGA) rung and the HSE03-1/3x DF<sup>189</sup> at the hybrid rung of DFT. The RPBE DF may be viewed<sup>239</sup> as a variant of the non-empirical GGA PBE DF<sup>154</sup>, with the RPBE DF originally designed to improve the description of chemisorption energies of atoms and molecules on metal surfaces. Hammer *et al.* constructed the RPBE DF in such a way that the same non-empirical constraints imposed on the PBE-DF are also imposed on RPBE<sup>239</sup>. Importantly for metals, the recovery of the uniform electron gas limit at zero gradient of the density is included<sup>255</sup>. In general, we can consider the RPBE functional as more 'repulsive' than the PBE functional, i.e., the RPBE barriers for both gas-phase reactions and dissociative chemisorption reactions on metals are higher than the PBE DF barriers<sup>135,256</sup>. This generally results in lower reactivity when describing a gas-metal system with the RPBE functional<sup>56</sup>.

The HSE03-1/3x DF is a screened hybrid functional. It is a hybrid DF because a fraction of exact exchange (also somewhat ambiguously called Hartree-Fock exchange) is admixed to the GGA exchange<sup>152</sup>. It is screened because the exact exchange is turned off at long range. This means that at long range the functional behaves like a PBE DF<sup>154</sup>, whereas at short range it will behave as a PBE0-like hybrid DF<sup>153</sup>. The screening of the exact exchange in metals is vital, because without it a myriad of descriptive issues can occur, not the least of which is a reduction of the density of states of the electrons at the Fermi level<sup>158</sup>.

The HSE03-1/3x DF is similar to the original HSE03 DF<sup>189,190</sup>, i.e., to the HSE03 DF that has been corrected for an implementation error<sup>190</sup>. The HSE03 DF only differs from the better-known HSE06 functional through the use of a slightly different screening range parameter<sup>189,190</sup>. The difference between the HSE03-1/3x DF and the HSE03 DF in Ref. <sup>189</sup> is that we implemented a different maximum fraction of exact exchange ( $\alpha$ ). The  $\alpha$ -values for PBE0 and HSE03 were originally set to 1/4, whereas we use  $\alpha = 1/3$ . Increasing the exact exchange is an accepted approach to improve the performance for gas-phase reaction barrier heights<sup>139,257</sup>, and was thus used already in earlier work on O<sub>2</sub> + Al(111)<sup>124</sup> to improve over the description of the O<sub>2</sub> on Al(111) system obtained with the original HSE03 functional.

Here a non-self-consistent field (NSCF) HSE03-1/3x@RPBE calculation is performed by first initialising and converging a self-consistent field (SCF) calculation with the lower level RPBE functional to obtain a well-converged electron density. The higher level HSE03-1/3x density functional<sup>189</sup> is then applied once to this density (using its Kohn-Sham wavefunction) to compute the HSE03-1/3x@RPBE energy. Vital to achieving an accurate and converged result in this type of calculation is that a high enough level of convergence is achieved for the energy (and thereby the density) at the lower (RPBE) level of theory. We have found that this requires a tougher energy tolerance than usually needed in a self-consistent calculation, presumably because the RPBE density is not equal to the density that corresponds to the variational minimum energy that would be obtained with the self-consistent HSE03-1/3x functional.

#### 3.2.3 Computational details

All DFT calculations are performed with the Vienna Ab initio Simulation Package (VASP) version 5.4.4 $^{200,258-262}$ . The initial SCF GGA spin-polarised DFT calculations are done with the RPBE $^{239}$  functional. The calculations use a 2x2 Al(111) supercell with 4 layers and a vacuum distance of 10 Å. The Al surface is described by a lattice constant of 4.022 Å and interlayer distances of  $d_{12} = 2.356$  Å,  $d_{23} = 2.248$  Å, and  $d_{34} = 2.353$  Å, which are the same as the values used in Ref.  $^{124}$  for the SCF HSE03-1/3x DF calculations. A plane wave cut-off energy of 400 eV and an 8x8x1  $\Gamma$ -centred k-point grid is used. The core electrons are represented by the projector augmented wave (PAW) $^{199}$  method, and first-order Methfessel-Paxton smearing with a width of 0.2 eV is employed to improve convergence. The energy convergence criterium for the RPBE functional is set to  $10^{-9}$  eV. This stringent convergence criterium is specifically chosen with the erratum $^{145}$  on the work of reference  $^{124}$  in mind and is discussed further in Section 3.3.1.

To complete an NSCF HSE03-1/3x@RPBE calculation we perform another single-point calculation by applying the HSE03-1/3x DF one time to the pre-converged RPBE density. This calculation uses mostly the same DFT settings as the SCF GGA single-point calculations. The notable difference, however, is the use of the screened hybrid HSE03<sup>189</sup> functional with an exact exchange fraction of 1/3. (see

also Section 3.2.2) In this calculation, the SCF-RPBE density and Kohn-Sham wavefunction of the previous calculation are used, and the HSE03-1/3x is not applied in a self-consistent manner but only once to compute the screened hybrid energy from the converged RPBE density.

## 3.2.4 Constructing the PES

In the most common approach to performing quasi-classical trajectory (QCT) dynamics calculations a continuous and global PES is used that is fitted to electronic structure calculations using the DF of which the accuracy is evaluated. As discussed in Section 3.2.1, the PES in this work is dependent on the six degrees of freedom of the diatomic (O<sub>2</sub>) molecule. A continuous representation of this six-dimensional PES is obtained by applying the corrugation-reducing procedure (CRP)<sup>201,202</sup> to a grid of DFT single-point energies. In this approach, atom-surface PESs are subtracted from the full 6D PES such that the 6D rest function is less corrugated and easier to interpolate. In previous studies, this procedure led to off-grid interpolation errors that were no larger than 30 meV  $^{202}$  (2.9 kJ/mol) and 0.7 kcal/mol  $^{115}$  (2.9 kJ/mol). Moreover, in the work of Smeets et al. a large test set of 4900 samples was used to test the interpolation error of the CRP method<sup>130</sup>. This resulted in a root mean squared error (RMSE) of 31 meV (3.0 kJ/mol). However, this RMSE was reduced to 8 meV (0.8 kJ/mol) if the interaction energies between molecule and metal were smaller than 4 eV 130. For  $O_2 + Al(111)$ , most interaction energies are within 4 eV in the configuration space relevant to the reaction dynamics (see also Figure 3.7 in Section 3.3.4). Furthermore, **Table 3.3** in Section 3.5.1 shows a comparison of reaction barrier energies extracted from the CRP PES (as also shown in Table 3.2 in Section 3.3.4) with values directly calculated for the corresponding CRP barrier geometries using DFT (the NSCF HSE03-1/3x@RPBE DF). The RMSE of 0.61 kJ/mol is consistent with the value of 0.8 kJ/mol for total interaction energies smaller than 4 eV in the earlier cited study, with the largest deviation between a CRP and a DFT barrier being about 3.0 kJ/mol, in what is a clear outlier in the set. The CRP procedure used in this chapter is along similar lines as in e.g. the work of Ref. 263, except for two distinctions.

First, we did not employ an equidistant (r, Z)-grid. Instead, we used a similar grid as used in Ref. <sup>124</sup> for the calculations with the SCF HSE03-1/3x functional, i.e., Z = [1.00, 1.50, 2.00, 2.25, 2.50, 2.75, 3.00, 3.25, 3.50] Å, and r = [1.0, 1.1, 1.15, 1.175, 1.2, 1.225, 1.25, 1.3, 1.4, 1.5, 1.6] Å. This grid limits the number of single points necessary for a good representation whilst maintaining high accuracy for the description of the molecule in the gas-phase and at the transition sate (TS). We opted to use the same grid as the earlier  $O_2 + Al(111)$  work of Gerrits  $et\ al$ . to enable an optimal comparison with the calculations using the SCF HSE03-1/3x DF PES, in the sense that differences should not be attributable to the use of a different grid of points.

The second distinction is that, similar to reference <sup>124</sup>, we employ the atomic 3D PES computed with the MS-RPBEI DF<sup>128</sup> instead of an atomic PES obtained with the (NSCF) HSE03-1/3x functional. This is done to maintain comparative PESs between the NSCF and SCF DF. Regardless, the three-dimensional atomic PES will not influence the 6D PES itself as long as the 3D potential is physically reasonable, since the 3D atomic PES is used only to decrease the corrugation of the 6D PES during the fitting procedure, as also discussed in Ref. <sup>124</sup>.

## 3.2.5 Quasi-classical trajectory calculation

A global PES as produced by the CRP allows for performing quasi-classical trajectory (QCT)<sup>210,211</sup> dynamics calculations, along similar lines as in previous work<sup>124,125,130</sup>. With QCT we take into account the molecule's initial zero-point energy, after which the molecular trajectory is propagated classically in time. If the bond length of  $O_2$  exceeds the threshold of  $1.59 \, \text{Å}$  in a trajectory, we count that trajectory as reacted. If the value of Z increases beyond the value of Z at the starting point of the trajectory (i.e., if  $Z > 5.0 \, \text{Å}$ ) we consider the molecule to be scattered. The reaction probability ( $P_r$ ) is calculated using:

$$P_r = \frac{N_r}{N_{total}} \tag{3.2}$$

where  $N_r$  is the number of trajectories that correspond to a reaction and  $N_{total}$  is the total number of trajectories run.

Two types of molecular beams were simulated for this chapter. This first type is used to simulate the experiments of Österlund et al.<sup>224</sup>, for which supersonic molecular beams with a nozzle temperature  $(T_N)$  equal to room temperature, i.e., 300 K, were used. In simulating the experiments the vibrational temperature of the molecules can be taken equal to the value of  $T_N$  in the experiments<sup>224</sup>. Due to the high rotational cooling in the oxygen molecular beams employed, the rotational temperature of  $O_2$  is only  $9K^{264}$ , resulting in a rovibrational state population presented in Table 3.1 (see Refs. 130,136 for more information). In the QCT calculations, we used a single value for the incidence energy of the molecule and allowed initial states with v = 0 - 3, and i = 1 - 49 to be populated. However, **Table 3.1** shows that O<sub>2</sub> molecules in a beam with  $T_N = 300 \text{ K}$  mostly occupy the rovibrational ground state (v=0, j=1). Note that we only consider the odd j states, because the even j states are forbidden according to nuclear spin statistics<sup>173</sup>. For this beam simulation, we ran 10,000 trajectories for each incidence energy to compute the reaction probability  $(P_r)$  per incidence energy with converged statistics.

**Table 3.1**: Rovibrational state population in an  $O_2$  molecular beam with a nozzle temperature of 300 K.

v state	j state	Rovibrational energy (eV)	Population
0	1	0.10687	80.6546 %
0	3	0.10865	18.8495 %
0	5	0.11186	0.47049 %
0	7	0.11650	0.00160 %
1	1	0.31449	0.02632 %
1	3	0.31626	0.00627 %
1	5	0.31944	0.00016 %

The second type of beam is used to simulate the experiments of Kurahashi and Yamauchi<sup>227</sup>, for which we employed a state-specific initial condition of v=0, j=1, with appropriate averaging over  $m_j=-1$ , 0, 1, according to the particular experiment simulated. We ran 2800 trajectories per incidence energy to compute the sticking probability. We then use the  $m_j$  state-specific reaction probabilities and the equations provided in the work of Kurahashi and

Yamauchi<sup>227</sup> to compute the reaction probabilities measured for particular rotational alignments. We refer the reader to reference <sup>227</sup> for the details.

#### 3.2.6 Hole model

The hole model<sup>254</sup> is a method to compute the sticking probability from the barrier corrugation and anisotropy without the usage of dynamics<sup>56</sup>. In this chapter we used the well-defined NSCF PES to compute the reaction, or sticking, probability, as described by the hole model<sup>56,254</sup>:

$$S_{0}(E_{mol}) = \frac{\int H\{E_{mol} - E_{B}(X, Y, \theta, \varphi)\} dU dV d\cos(\theta) d\varphi}{\int dU dV d\cos(\theta) d\varphi}$$

$$H\{\Delta E\} = \begin{cases} 1 \text{ if } \Delta E \ge 0 \\ 0 \text{ if } \Delta E < 0 \end{cases}$$
(3.3)

Here  $E_{mol}$  is the sum of the internal energy of the molecule (as defined by the temperature of the molecular beam) and the incidence energy of the molecule, and  $E_B(X, Y, \theta, \varphi)$  is the energy of the barrier for a given molecular geometry  $(X, Y, \theta, \varphi)$ .

In practice, we opt to use a Monte-Carlo-like approach to solving this integral. Analogously to Section 3.2.5, we compute the reaction probability as Equation 3.2, though now we do not use quasi-classical trajectory outcomes but distinct samples such that:

$$P_{r}(E_{i}) = \frac{N_{r}(E_{i})}{N_{total}} = \frac{\sum_{j}^{N_{total}} H\{E_{j}^{mol}(E_{i}) - E_{j}^{B}(U_{j}, V_{j}, \cos(\theta)_{j}, \varphi_{j})\}}{N_{total}}$$

$$E_{j}^{mol}(E_{i}) = E_{i} + E_{j}^{vibration} + E_{j}^{rotation}$$
(3.5)

where  $E_i$  is the incidence energy of the molecule,  $E^{vibration}$  and  $E^{rotation}$  are the vibration energy and rotation energy of the molecule for each sample j chosen randomly via the  $T_N=300K\,\rm O_2$  molecular beam population distribution (see also **Table 3.1**),  $N_{total}$  is the total number of samples used, H is the same Heaviside function as in Equation 3.4, and U, V,  $cos(\theta)$ ,  $\varphi$  are chosen randomly from uniform distributions for each j as defined in Section 3.2.1 (Note that in Equations 3.5 we use the U, V coordinates instead of X, Y see also Section 3.2.1). If  $N_{total}$  is chosen to be large enough (here it is chosen to be  $10^{\circ}$ ) Equation 3.5 should approach the results of Equation 3.3.

For each sample j, a molecular energy and molecular geometry (U, V,  $\theta$ ,  $\varphi$ ) are thus chosen according to the same initial conditions as in the QCT calculations. The geometry is used to compute the reaction barrier in r and Z via a simple two-dimensional barrier searching algorithm applied to the (NSCF) PES. The barrier search is in principle a basic saddle-point searching algorithm, assuming that only one saddle-point, or barrier, will exist per r, Z-elbow cut of the PES. The saddle points are found by starting a modified Powell method<sup>265,266</sup> root finding algorithm on the Jacobian of the two-dimensional (r, Z) PES from an initial guess on the elbow. This critical point is then verified to be a saddle point via a second-order derivative test with the hessian of the two-dimensional (r, Z) PES on the critical point (i.e., the discriminant of the hessian needs to be smaller than zero). If the critical point is not a saddle point, a new root search in the Jacobian is started from a different initial guess. This algorithm is basic but robust if the corrugation of the PES not to large so that extra critical points or saddle points are not present (to avoid the occurrence of false critical or saddle points).

#### 3.3 Results and discussion

Below the results of this chapter are presented. This is done with a few subsections. The first, i.e., section 3.3.1 discusses the need for stringent convergence of the RPBE density. Section 3.3.2 then follows this by presenting the sticking results from QCT calculations and comparing those results to the SCF HSE03-1/3x results, and other previous theoretical and experimental work. Section 3.3.3 then briefly discusses the sticking probability of rotationally resolved  $O_2$  molecules. This is followed by Section 3.3.4 where the differences in sticking probability are related to the differences in the PESs of both the SCF and NSCF DF. Lastly, in Section 3.3.5 the sticking results computed with the hole model are presented and analysed.

## 3.3.1 Converging a non-self-consistent field DFT calculation

As discussed in Section 3.2.2 it is important to achieve a high convergence of the DFT energy in the lower rung calculation of the electron density, to ensure that this density is stable. We found this to be particularly true for geometries in

which O<sub>2</sub> is still far away from the Al(111) surface. The NSCF energies can be quite dependent on the convergence of the GGA RPBE density used to evaluate the HSE03-1/3x@RPBE DF. An example of potential problems with less converged densities is shown in Figure 3.2. In this figure three different cuts through the potential energy surface are shown, plotting the total energy value of  $O_2$  + Al(111) for different bond lengths of  $O_2$  in the gas-phase, i.e., at 5.0 Å above the surface. In Figure 3.2A, results obtained with the SCF HSE03-1/3x functional are shown for an energy tolerance  $\Delta E_{Tol} = 10^{-5} \text{ eV}$ . In Figure 3.2B and C results obtained with the NSCF HSE03-1/3x@RPBE functional are shown for the RPBE tolerance of  $\Delta E_{Tol} = 10^{-5}$  eV in panel **B** and  $\Delta E_{tol} = 10^{-9}$  eV in panel **C**. Figure 3.2 clearly shows that obtaining accurate and converged results with the NSCF calculations requires a much lower value of  $\Delta E_{Tol}$  in the GGA primer calculation (a better-converged GGA electron density) than needed in an SCF calculation. As also discussed in Section 3.2.2. we attribute the much larger dependence of the NSCF energy on small changes in the GGA density to the GGA electron density probably not being equal to the electron density corresponding to the variational minimum for the higher-level functional. In this situation, one would expect to see a much larger dependence of the energy on small variations in the density.

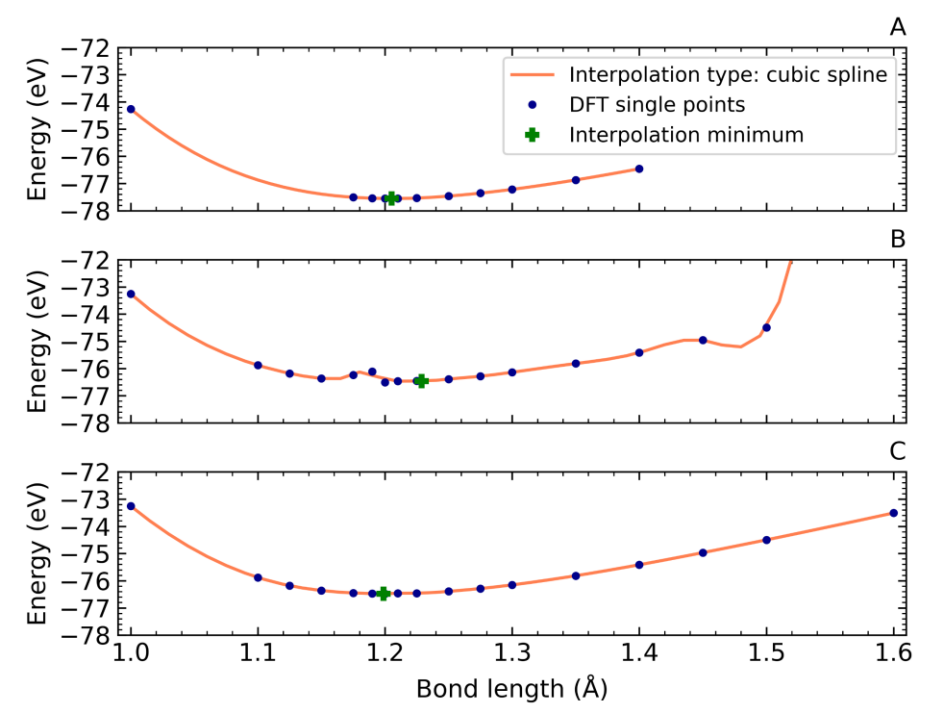


**Figure 3.2**: Three (cubic spline interpolated) potential energy cuts for  $O_2$  at 5 Å above the Al(111) surfaces, where all degrees of freedom are kept constant except for the oxygen bond length; **A**: HSE03-1/3x with an  $\Delta E_{Tol}$  of 10<sup>-5</sup> eV; **B**: NSCF HSE03-1/3x@RPBE with RPBE with an  $\Delta E_{Tol}$  of 10<sup>-5</sup> eV; **C**: NSCF HSE03-1/3x@RPBE with RPBE with an  $\Delta E_{Tol}$  of 10<sup>-9</sup> eV.

## 3.3.2 The reaction probability

In **Figure 3.3** the reaction probability computed with the NSCF hybrid functional (HSE03-1/3x@RPBE) is plotted as a function of incidence energy. We compare these results with reaction probabilities computed with SCF HSE03-1/3 $x^{124}$ , wavefunction theory embedded in DFT<sup>230</sup>, RPBE<sup>231,240</sup>, MS-RPBEI (a meta-GGA)<sup>124</sup>, and with experimental results<sup>224</sup>.

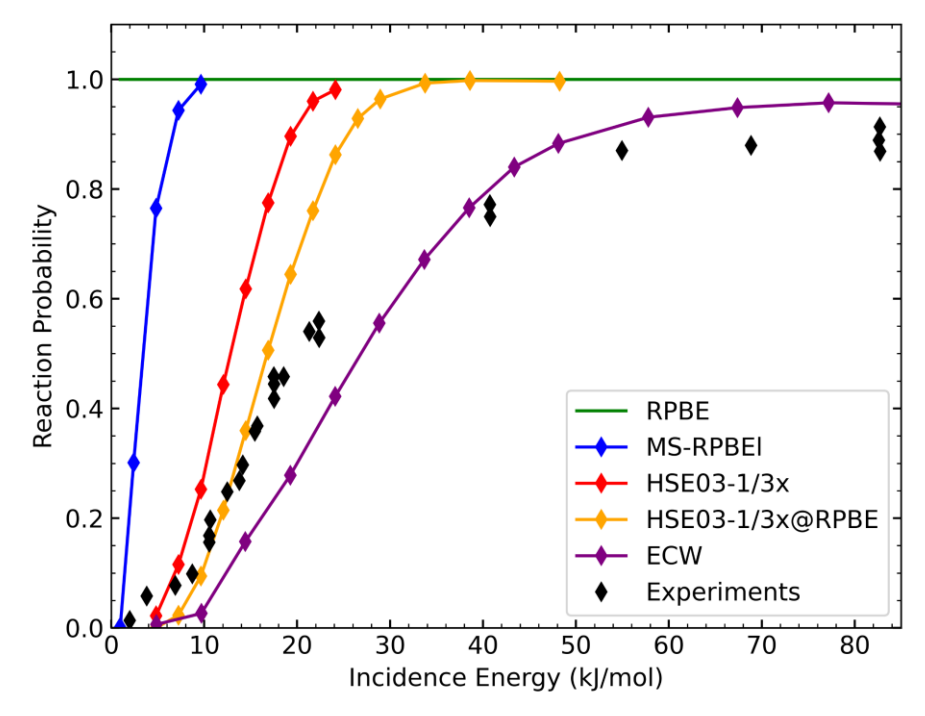


**Figure 3.3**: The reaction probability as a function of incidence energy as computed with the SCF HSE03-1/3x functional (red) $^{124}$ , the NSCF HSE03-1/3x @RPBE functional (orange), the embedded correlated wavefunction method (purple) $^{230}$ , and as measured in experiments (black) $^{224}$ , is compared with the reaction probability computed with the RPBE DF(green) $^{231,240}$ , and with the MS-RPBEI DF(blue) $^{124}$ .

Importantly, the NSCF results reproduce the SCF reaction probabilities within near-chemical accuracy (2 kcal/mol), but not within chemical accuracy (1 kcal/mol). The NSCF reaction probabilities appear to be shifted towards somewhat higher incidence energies. This energy shift is not constant: it is larger for higher incidence energies. The increase of the shift also means that the slope of the NSCF reaction probability curve is smaller. This somewhat reduced slope of the NSCF reaction probability curve corresponds to a small broadening of the sticking probability curve relative to the SCF results.

The difference in incidence energy dependency of the NSCF and SCF HSE03-1/3x sticking curves is visualised in **Figure 3.4** where we have plotted the incidence energy shift (or  $\Delta$ ) that the SCF HSE03-1/3x reaction probabilities would need to be shifted by to higher energies to morph into the NSCF HSE03-1/3x@RPBE

result. At low incidence energy, the energy shift required is small (2.4 kJ/mol) and well within chemical accuracy ( $1 \text{ kcal/mol} \approx 4.2 \text{ kJ/mol}$ ), but for larger incidence energies the required shift increases considerably (to 7.2 kJ/mol). Based on the energy shift we can say that the NSCF results reproduce the SCF results to within chemical accuracy up to an incidence energy of 14 kJ/mol. The energy shift of the NSCF curve also means that these results reproduce the initial onset of the experimental sticking curve less well (at  $E_i < 7 \text{ kJ/mol}$ ) than the SCF results, but the agreement of the NSCF results with experiments is unintentionally improved in the range of 10 - 23 kJ/mol (see **Figure 3.3**).

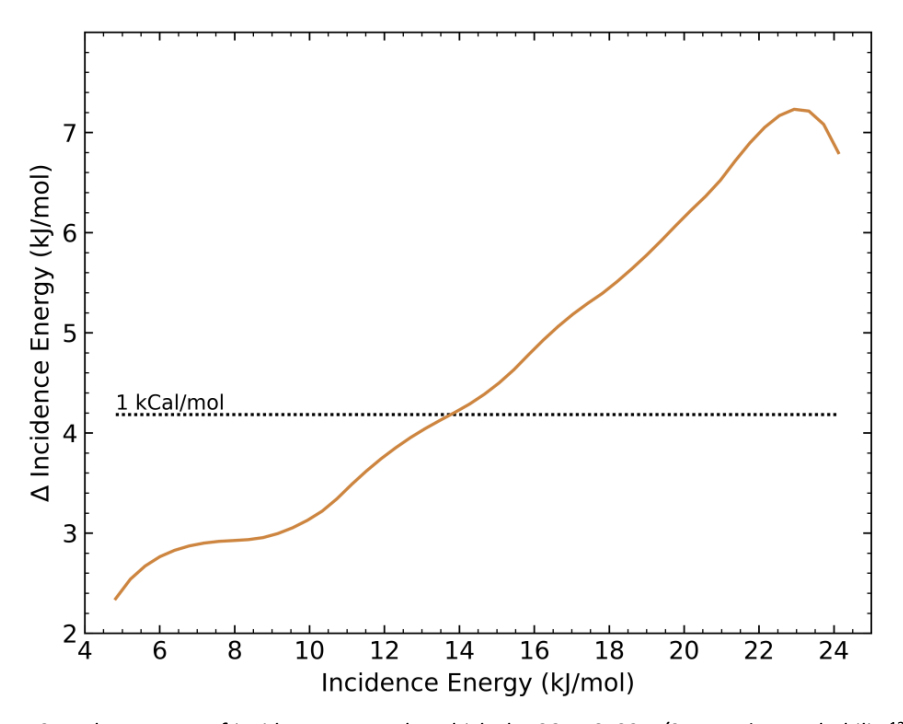


**Figure 3.4**: The amount of incidence energy by which the SCF HSE03-1/3x reaction probability<sup>124</sup> would have to be shifted to morph into the NSCF HSE03-1/3x@RPBE reaction probability curve is shown as a function of the incidence energy of the SCF reaction probability.

The disagreement between the SCF HSE03-1/3x and the NSCF HSE03-1/3x@RPBE results may be surprising when looking back at Ref. <sup>124</sup> where (originally) near exact agreement between SCF and NSCF barriers was reported. Such an agreement would suggest that reaction probability curves would also be

in excellent agreement with one another. However, this is, as shown above, not the case. The problem is resolved through the recent Erratum<sup>145</sup> published on the work of Ref. <sup>124</sup>, which corrected the reported NSCF 1D potential and further clarified the exact settings used for the published NSCF calculations. It appears that the input parameters in reference <sup>124</sup> for the SCF RPBE in the NSCF HSE03-1/3x@RPBE functional were set at values not yet sufficiently stringent to obtain a stable NSCF energy. The limited convergence of the GGA density likely resulted in energetic noise in the gas-phase description of the  $O_2 + Al(111)$  model (see also **Figure 3.2**). This, in turn, has most likely resulted in incorrect molecule-surface interaction energies, as an unstable result for  $O_2$  in the gas-phase was subtracted from the energy of the combined system. All in all, this resulted in a down-shifted barrier height, thereby presenting a too optimistic picture of the NSCF-screened hybrid DF barrier description.

We found that, when using a plane wave code like VASP for the O<sub>2</sub> on Al(111) system, only a small fraction of the computation time for an NSCF hybrid single point is spent on generating a well-converged SCF GGA density. A very stringent convergence setting in the SCF GGA calculation is therefore of little influence on the total computation time. Moreover, the computational cost of an NSCF hybrid single-point calculation is between  $1/20^{th}$  to  $1/200^{th}$  of the cost of a full SCF hybrid single-point calculation. It is, therefore, encouraging to see that the NSCFscreened hybrid results represent a considerable improvement over the RPBE GGA and the MS-RPBEI mGGA results<sup>124</sup> shown in **Figure 3.3**, at a computational cost that is more than an order of magnitude lower than the SCF hybrid DFT calculations. Specifically, we observe that a single application of the screened hybrid functional to a well-converged GGA (i.e., RPBE) density is capable of altering the sticking probability curve to a result much closer to the desired, experimental, outcome and reproduces the SCF Hybrid DF with near-chemical accuracy. This last point strengthens the argument made in earlier work<sup>124</sup> that the errors made with GGA functionals when describing systems with a low charge transfer energy, like the O<sub>2</sub> + Al(111) system investigated here, are likely to be mostly functional-driven, with only a small density-driven component.

It would obviously be more elegant if the NSCF results would reproduce the SCF results even more closely so that the HSE03-1/3x@RPBE results could be cast as

a very good approximation to the HSE03-1/3x results. In that case, our dynamics calculations would directly test the quality of the DF as used self-consistently, and the comparison with the experiment would be more telling of the quality of the functional itself. The remaining disagreement between SCF and NSCF results does suggest that the DF errors are not entirely functional driven, and that part of the GGA failure is due to errors in the GGA density. This then raises the question of how the density-driven part of the error is related to the system we are treating. Would the disagreement between NSCF and SCF-screened hybrid calculations, where the NSCF calculations are based on GGA densities, be smaller if the functionals were applied to systems with smaller charge transfer energies? And would electron densities from mGGA DFs improve the description further? It may be fruitful to explore the answer to these and other related questions, and thereby hopefully learn more about how problems with DFT are related to the type of system to which it is applied, and how such problems may be solved.

Nevertheless, the NSCF-screened hybrid results are in semi-quantitative agreement with experiments and reproduce the SCF results within near-chemical accuracy. This suggests that the NSCF approach could be used in explorative research aimed at extracting reaction barrier heights for difficult dissociative-chemisorption-on-metal systems (i.e., systems that require hybrid DF's for a proper description at great computational costs, with charge transfer energies < 7~eV). This way, hopefully, the best DFs for a given system can be identified in the same fashion as used earlier for 'easy' systems (with charge transfer energies > 7~eV), see Refs. S6,129. As discussed there, this would allow minimum reaction barrier heights to be extracted for such systems, as experimental reaction probability curves should only be reproduced if the barriers in the PES are correctly described (this argument can be based on the hole model 254, as also discussed in Ref. S6).

## 3.3.3 Sticking of rotationally aligned O<sub>2</sub>

In 2013 Kurahashi and Yamauchi showed that the sticking of  $O_2$  on Al(111) depends strongly on the alignment of the  $O_2$  molecule relative to the surface<sup>227</sup>. Using a single spin-rotational state-selected  $O_2$  beam their work differentiates the sticking between the two different DC mechanisms of  $O_2$  that are at play<sup>227</sup>.

Here the first mechanism is direct DC, which can occur when the molecule is parallel to the surface<sup>267</sup> e.g., in a helicoptering state. The second mechanism occurs when the molecule is mostly perpendicular to the surface, in which case abstraction can occur<sup>219,268–271</sup>. Kurahashi *et al.* showed that, for lower incidence energies of  $O_2$ , only a small fraction of the  $O_2$  reacts through the abstraction mechanism<sup>227</sup> (see also **Figure 3.5**).

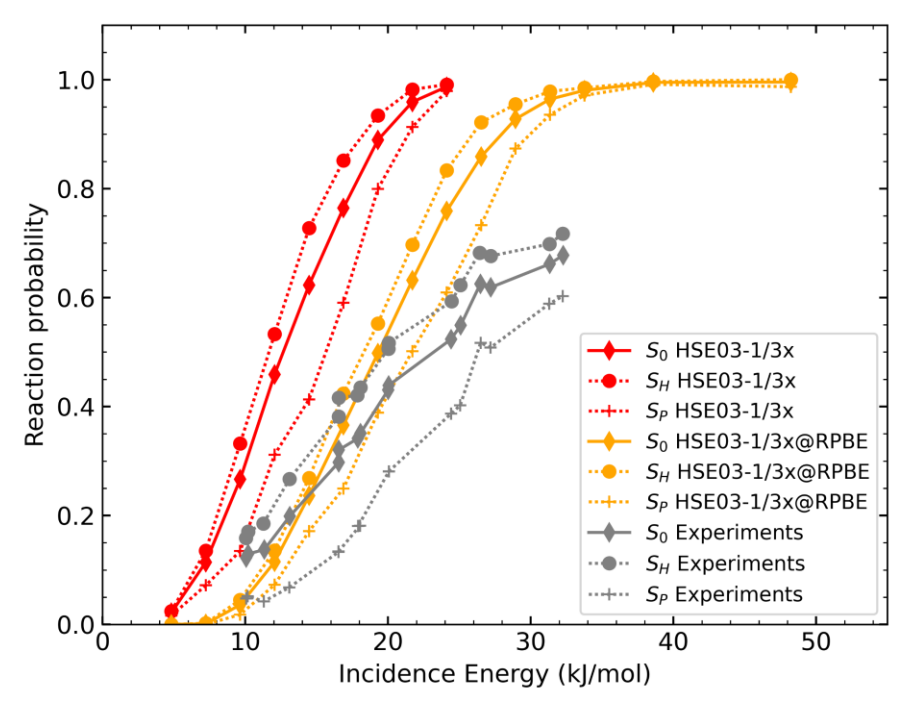


**Figure 3.5**: Total and rotationally resolved sticking curves as a function of incidence energy (kJ/mol) for molecular beams of  $O_2$  in the v=0, j=1 (V=0, J=2, K=1) state only; as computed with the SCF HSE03-1/3x (red)<sup>124</sup>, and NSCFHSE03-1/3x@RPBE (orange) functional are compared with the measured reaction probabilities(grey)<sup>227</sup>. Diamonds and solid lines represent the unaligned state reaction probability ( $S_0$ ). The circles represent the sticking curve of helicoptering molecules that rotate in a plane parallel to the surface ( $S_H$ ) and the plus symbols represent the sticking of molecules that are preferentially aligned perpendicular to the surface ( $S_P$ ).

Similarly to Ref.  $^{124}$ , we simulate the orientationally aligned state-selected  $O_2$  experiments using our NSCF hybrid functional. We ran quasi-classical trajectories for each of the three specific rovibrational states (v=0, j=1, and  $m_j=-1$ , 0, 1) and used Equations 1-5 from the work of Kurahashi $^{227}$  to combine the  $m_j$  state-specific reaction probabilities to obtain sticking probabilities for the two orientationally aligned states prepared experimentally. Note that in

spectroscopic terms the rovibrational spin state of  $O_2$  is indicated by V=0, J=2, K=1, and  $M_K=-1$ , O, O, O is the O ought not to be confused with O, which is the angular momentum associated with the rotation of the molecule. The sticking probabilities computed for the two rotationally aligned states with the SCF HSE03-1/3x DF (red)<sup>124</sup>, and NSCF HSE03-1/3x@RPBE DF (orange) are compared with experiment (grey)<sup>227</sup> in **Figure 3.5**.

# 3.3.4 The role of the energetic corrugation of the barrier height

To explain the difference between the NSCF and SCF reaction probabilities, we tabulated the reaction barriers of both DFs, and their difference ( $\Delta$ ) for each elbow cut used to fit the CRP PES in **Table 3.2**, and we plotted a sample set of the barrier heights for both approaches (SFC and NSCF) in **Figure 3.6**. This figure (as well as **Table 3.2**) shows that all barriers generated using the NSCF approach (orange) are higher in energy than those generated by the SCF approach (red). However, it remains hard to discern a pattern to the shifts in barrier height. There seems to be no constant shift or addition, and the barriers also do not universally scale with a single scalar. There also does not seem to be a clear dependence of the shifts on barrier geometry, nor does the type of surface site seem to influence the shift of the barrier height. However, a consistent trend is that large barriers obtained with the SCF functional correlate with large barriers computed with the NSCF functional and with larger shifts.

The lowest barrier height seen in **Table 3.2** and **Figure 3.6** (Bridge-P,  $\varphi$ :  $O^{\circ}$ ) corresponds roughly with the sticking curve onset seen in **Figure 3.3**. The minimum SCF barrier height is about  $4.7 \, kJ/mol$  and the SCF sticking onset is at approximately the same incidence energy. The NSCF minimum barrier can be found at around  $6.6 \, kJ/mol$  and the onset of the NSCF sticking curve is somewhat below  $7 \, kJ/mol$ . From these results, it is clear that an incidence energy approximately equal to the minimum barrier height is enough to initialise dissociation for a parallel-oriented  $O_2$  molecule (see also Section: 3.3.3.). This is also in agreement with the barriers to dissociation generally being in the entrance channel (see also the potential elbows in **Figure 3.7** for the barrier locations) of the reaction, with Polanyi's rules<sup>273</sup> dictating that the  $10.28 \, kJ/mol$ 

of initial vibrational energy (for the ground state  $O_2$ , see also Section 3.2.5., **Table 3.1**) is not used to overcome this barrier. As such, for a molecular beam with a rotational temperature of only  $9 K (0.03 \, kJ/mol \, \text{for } j=1, 80\% \, \text{populated}$ , see **Table 3.1**) the incidence energy should be the only significant component of the molecule's energy that can be used to overcome the barrier.

**Table 3.2**: Barrier heights computed with the SCF HSE03-1/3 $x^{124}$ , the NSCF HSE03-1/3x@RPBE DFs, and their difference ( $\Delta$ ) are presented for all elbow cuts used to fit the CRP PES. See **Figure 1.1B** for the name and location of the high symmetry sights; the  $O_2$  orientation is indicated with P(parallel) for  $\theta$ =90°, N(Normal) for  $\theta$ =0°, and T(Tilted) for  $\theta$ =45°.

High Symmetry geometry	SCF, HSE03-1/3x Barrier height ( <i>kJ/mol</i> ) <sup>124</sup>	NSCF HSE03-1/3x@RPBE Barrier height ( <i>kJ/mol</i> )	∆ Barrier height (kJ/mol)
Top N	26.8	29.8	3.0
Top P, φ: 0°	22.7	24.4	1.7
Top P, φ: 30°	22.5	24.4	1.9
Bridge N	19.5	25.5	6.0
Bridge P, φ: 0°	4.7	<u>6.6</u>	1.8
Bridge P, φ: 60°	19.6	29.7	10.1
Bridge P, φ: 90°	29.5	51.4	21.8
TtF N	22.9	29.1	6.2
TtF Τ, φ: 150°	26.0	38.0	11.9
TtF Τ, φ: 240°	12.5	16.7	4.1
TtF Τ, φ: 330°	14.4	16.6	2.2
TtF P, φ: 240°	23.6	28.7	5.1
TtF P, φ: 330°	10.7	12.8	2.1
TtH N	21.9	27.7	5.8
TtH Τ, φ: 30°	14.4	16.8	2.4
TtH Τ, φ: 120°	12.8	16.9	4.1
TtH Τ, φ: 210°	25.3	36.3	11.1
TtH P, φ: 30°	10.1	12.3	2.2
TtH P, φ: 120°	23.7	37.8	14.1
FCC N	26.9	38.5	11.6
FCC T, φ: 150°	24.6	32.5	7.9
FCC T, φ: 330°	<u>39.9</u>	<u>60.0</u>	20.1
FCC P, φ: 0°	11.5	13.5	2.0
FCC P, φ: 330°	12.4	14.6	2.2
HCP N	22.8	34.6	11.9
HCP Τ, φ: 210°	23.3	31.0	7.7
HCP Τ, φ: 30°	<u>39.9</u>	56.2	16.3
HCP P, φ: 0°	10.4	12.7	2.3
HCP P, φ: 30°	11.4	13.7	2.3

The barrier height analysis might additionally help with explaining the results of the sticking of rotationally aligned  $O_2$ , as the minimum barrier height is found for the parallel orientation above a bridge site, and barriers for the reaction with  $O_2$  normal to the surface are found at several kJ/mol higher energy. It is therefore not surprising that in the limit of low incidence energy the direct DC mechanism, in which the molecule is parallel to the surface, is favoured.

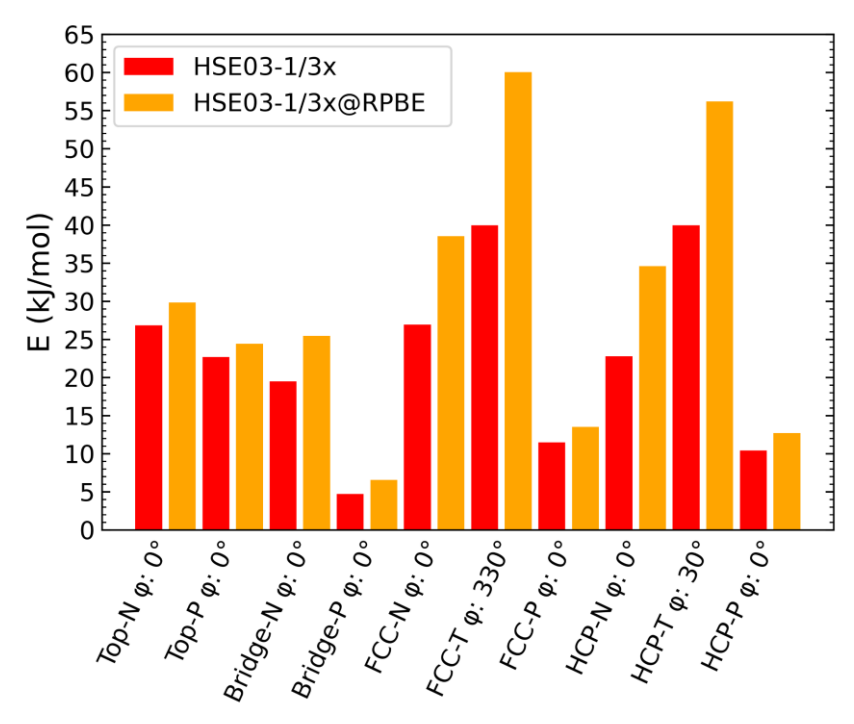


**Figure 3.6**: The barrier heights (in kJ/mol) calculated with the SCF HSE03-1/3x (red) and the NSCF (orange) HSE03-1/3x@RPBE functional are shown for a large set of different geometries. See **Figure 3.1** for the name and location of the high-symmetry sites. The  $O_2$  orientation is indicated with P(parallel) for  $\theta$ =90°, N(normal) for  $\theta$ =0°, and T(tilted) for  $\theta$ =45°.

The analysis of the barrier heights explains why the widths of the sticking probability curves differ for the NSCF and the SCF results. The energetic corrugation of the barrier height is increased with the NSCF approach over the SCF approach, because, as observed in **Figure 3.6** and **Table 3.2**, higher barriers in the SCF approach are correlated with larger positive energy shifts of the NSCF barrier heights relative to the SCF barrier heights. As a result, the difference between the minimum and maximum barrier height for HSE03-1/3x@RPBE in **Table 3.2** is much larger (*53.5 kJ/mol*) than the analogous difference for the self-

consistent HSE03-1/3x DF (*35.2 kJ/mol*), see also the underlined barrier heights in **Table 3.2**. The higher energetic corrugation of the barriers in the NSCF approach is likely the cause of the increased width (i.e., reduced slope) of the NSCF sticking curve relative to that of the SCF curve, as observed in **Figure 3.3**<sup>254</sup>.

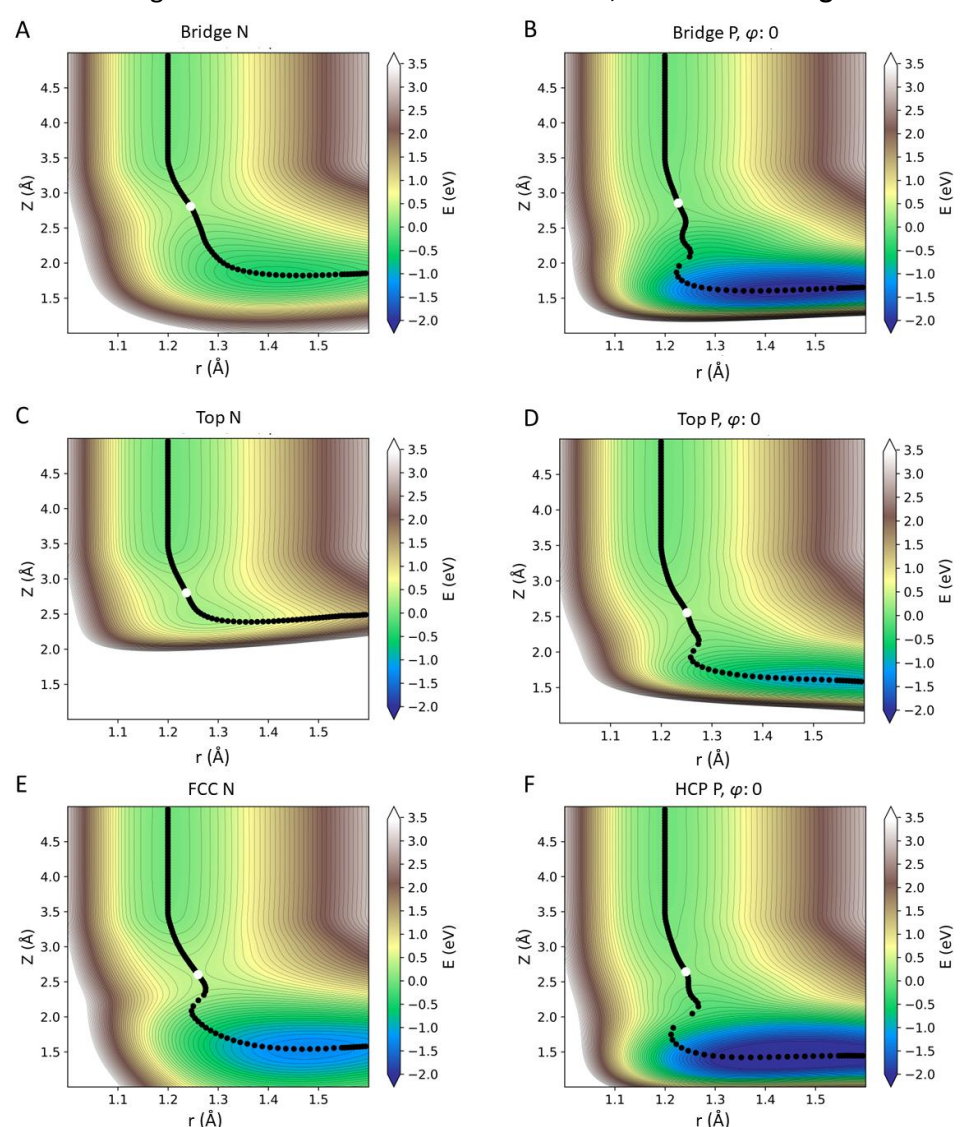


**Figure 3.7**: Set of 6 'elbow cuts', showing slices through the PES as a function of the molecule's bond length (r) and the distance of  $O_2$  to the surface (Z) for six different geometries (sampling four different surface sites and two different molecular orientations). Contour lines are separated by 2 kcal/mol. Each elbow shows the approximate minimum energy path with black dots. The white dots show the location of the transition state in reduced dimensionality; **A**: Bridge N, **B**: Bridge P- $\varphi$ : 0°, **C**: Top N, **D**: Top P- $\varphi$ : 0, **E**: FCC N, **F**: HCP P- $\varphi$ : 0°.

The rather small change of the QCT reaction probability curve width despite the substantial increase of the barrier corrugation (obtained with the NSCF potential) raises concerns about a suggestion made in earlier work<sup>124</sup>. Increasing the energetic corrugation of the barrier height and increasing the anisotropic dependency of the barriers by adding in the attractive van der Waals interaction has been suggested as a way to resolve the difference in slope between the sticking probability curve computed with the HSE03-1/3x functional and the experimental curve<sup>124</sup>. However, with our NSCF approach, we have already inadvertently but considerably changed the barrier corrugation and anisotropy and this is seen to lead only to a minor increase in the width of the sticking curve. Yet, it is unclear what effects Van der Waals correlation would have on the dynamics of the reaction. For future theoretical work of O<sub>2</sub> on Al(111), it may still be relevant to not only attempt to increase the energy corrugation or affect the dynamics with the addition of Van der Waals correlation but also to look more closely at non-adiabatic effects that may occur in this system, which may also affect the slope of the sticking curve: Systems in which charge transfer is likely, like  $O_2$  on Al(111), may also be more prone to electron-hole-pair excitation 124,136,170,171. Additionally, it is not yet known whether or not the thermal displacement of the surface atoms could influence the reaction barriers or whether the sudden approximation will hold for O2 on Al(111)<sup>221,274,275</sup>. Therefore, we might also need to study the effect of thermal displacements of the surface atoms and of energy transfer to surface atom motion. Conversely, experiments show little influence of the surface temperature on the reaction probability<sup>224</sup> indicating a limited influence of surface motion. However, this has not yet been checked with theory, nor do we know whether the reaction probability can be diminished by energy dissipation to the surface atoms at higher incidence energies. Further theoretical work should address these points.

Although the change in the barrier corrugation appears to be considerable, as stated before the change of the slope (or width) of the reaction probability curve is rather small in **Figure 3.3**. This could also suggest that dynamical effects such as steering play an active role in the reaction, as was also previously suggested by Carter and co-workers<sup>229,230</sup>. Steering effects have also been indicated in other DC systems of slowly rotating molecules incident on a surface at low translational

energies<sup>59,276–278</sup>. The importance of steering effects can be investigated with the hole model, as will now be discussed.

#### 3.3.5 The hole model

An interesting way to test for the importance of dynamical effects is by applying the hole model<sup>254</sup>. Put simply, the hole model states that for a particular geometry, a reaction will occur if the translational plus internal energy of the molecule is equal to or greater than the barrier height<sup>56</sup>. Using the hole model the reaction probability can be computed using Equation 3.3. The method does not include any dynamical effects, but it does include the effect of the distribution of the initial rovibrational  $O_2$  states through its dependence on the initial energy of the molecule. It also includes the effects of the minimum barrier height, the corrugation of the barrier, and the anisotropy of the barrier. The Monte-Carlo-like implementation of the hole model we use is described in detail above, in Section 3.2.6.

In Figure 3.8 we show reaction probability curves computed with four different interpretations of the hole model, where each point on the curve is based on  $10^6$  samples of initial  $O_2$  energies and geometries taken on the HSE03-1/3x@RPBE PES, and compared them to QCT results obtained with the same PES. The uppermost curve implements the regular hole model (i.e., initial vibrational energy included, gold upward triangles interpolated by a dotted line), and the lowest curve shows hole model results where we excluded the vibrational energy of the molecule (light green downward triangles, dotted line). Lastly, Figure 3.8 presents these same reaction probability curves shifted horizontally with  $6.73 \ kJ/mol$  and  $-3.54 \ kJ/mol$  respectively (darker colour variants and dashed lines) to achieve optimal agreement with QCT results.

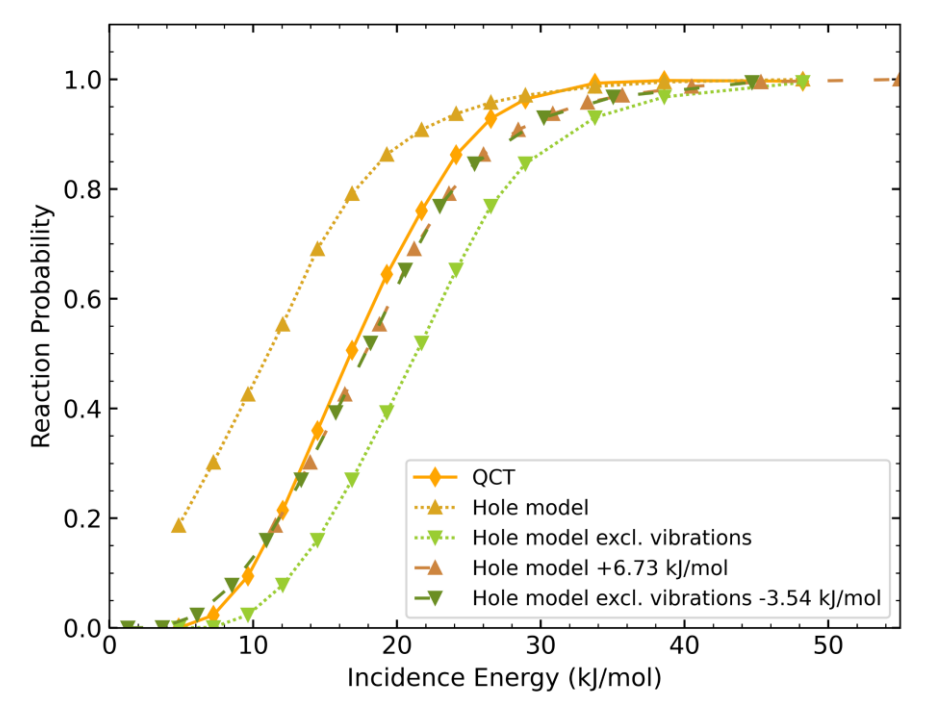


**Figure 3.8**: Reaction probability as a function of incidence energy for the HSE03-1/3x@RPBE DF PES. The results of the QCT method (orange diamonds and solid line), the hole model including vibrational energy (triangles down), and the hole model excluding vibrational energy (triangles up) are shown with dotted lines. The dashed lines represent shifted reaction probabilities obtained with these versions of the hole model. The shift in incidence energy is 6.73 kJ/mol to the right for the hole model including vibrational energy, and 3.54 kJ/mol to the left for the hole model excluding vibrational energy.

The agreement between the regular hole model and the QCT results is reasonable, although it seems that the regular hole model yields a slightly wider reaction probability curve, and systematically overestimates the QCT reaction probability. However, this overestimation is not unexpected. The hole model assumes that all of the internal energy of the molecule is available to overcome the reaction barrier. This includes zero point energy (ZPE), which cannot all be used to overcome a barrier. Additionally, we know from Polanyi's rules<sup>273</sup> that converting vibrational energy into motion along the reaction path should be inefficient for an early barrier reaction. We therefore also included hole model results where we excluded the initial vibrational energy from the total energy of  $O_2$ , which leads to a reaction probability curve that is shifted to higher energy by

about 10 kJ/mol relative to the regular hole model curve. This shift is approximately equal to the vibrational energy of  $O_2$  in v=0 (99% of  $O_2$  is in v=0 at  $T_N=300$  K, see **Table 3.1**). These results, predictably, now underestimate the QCT reaction probability. Excluding all vibrational energy of the molecule is of course a slight overcorrection on Polanyi's rules, as the early barrier is often found at slightly expanded bond lengths (see also **Figure 3.7**). It is also an overcorrection for the ZPE, as the gas-phase ZPE of the  $O_2$  molecule is not the same as, and typically higher than, the ZPE of  $O_2$  at the TS in reduced dimensionality if only r and Z are considered.

To best evaluate the different hole model results we shifted the two different hole model curves horizontally to match the onset of the QCT curve as well as possible (the lowest value of the regular hole model is at a reaction probability of 0.186, thus we match the curves in  $E_i$  to this value of the reaction probability) Figure 3.9 and Figure 3.10 in the Section 3.5.2 show the continuous energy shifts required to superimpose the reaction probability curves for the incidence energy range of 5-30 kJ/mol similar to Figure 3.4). Matching the curves with the QCT results required shifting the regular hole model curve to higher energies by 6.7 kJ/mol, and shifting the hole model curve excluding the effect of the vibration by 3.5 kJ/mol to lower energies. Based on this we can say that the amount of vibrational energy used to overcome the barrier is roughly one-third that of the vibrational energy of O<sub>2</sub> in the gas-phase. Interestingly, shifting the hole model curves like this reveals a small but clear difference between the widths (or slopes) of the reaction probability curves: the hole model reaction probability curves are broader than the QCT reaction probability curve. This suggests that dynamical effects, possibly related to steering, occur and that these favour the dissociation of O<sub>2</sub> on Al(111) most at the low incidence energies where there is time for the forces acting on the molecule to steer it to more favourable geometries for reaction. At the same time, this effect appears to be rather small, suggesting that the hole model can be used as a computationally cheaper screening tool to test electronic structure methods for  $O_2$  + Al(111), or more generally systems where dynamical effects are limited. The use of the hole model allows for savings on computation time not only because dynamics calculations can be skipped, but also because the PES is not required beyond the barrier geometries (i.e., in the exit channel).

## 3.4 Conclusions

 $O_2$  + Al(111) is a benchmark system for modelling  $O_2$  dissociation on metal surfaces and oxide formation. Thus far, the theoretical community has not been able to come to a consensus on the fundamental mechanisms at play in the dissociative chemisorption of  $O_2$  on Al(111). One underlying cause is that GGA functionals (the most commonly used functionals in the study of gas-metal surface interactions) are unable to describe barriers of  $O_2$  dissociative chemisorption on metals correctly if the charge transfer energy ( $\Phi$  - EA) is smaller than  $T eV^{124}$ . Recent work<sup>124</sup> suggested that using a screened hybrid DF will yield better results than GGA functionals even if the screened hybrid DF is applied in an NSCF manner to a GGA electron density. Here we tested this idea for  $O_2$  + Al(111).

Our results show that the NSCF approach to a screened hybrid density functional (DF) (HSE03-1/3x@RPBE) is indeed a major improvement over GGA (RPBE) or even meta-GGA (MS-RPBEI) DFs for describing the dissociative chemisorption of  $O_2$  on Al(111), while also limiting the extra computational cost by at least one order of magnitude compared to fully self-consistent hybrid calculations. The sticking curves generated with the NSCF-DF are within near chemical accuracy of the SCF-DF results for both full molecular beam simulations and rotationally aligned sticking. Moreover, with the NSCF approach, the quantitative agreement with experiments was inadvertently improved over that obtained with the SCF HSE03-1/3x approach.

The NSCF-screened hybrid DF was not able to exactly reproduce the SCF-screened hybrid functional results. The onset of the NSCF DF reaction probability at low incidence energy is within chemical accuracy of the SCF results. The NSCF approach leads to a slightly reduced slope of the reaction probability curve, resulting in a slightly increased disagreement with the SCF results at larger incidence energies. This can be traced back to the differences in barrier heights between the SCF and NSCF methods. The NSCF barrier heights are shifted to higher energies relative to the SCF barriers by a minimum of 1.8 kJ/mol, with the difference increasing with the SCF barrier height. Overall the anisotropic variation of the barrier height and the corrugation of the barrier height have been increased by the NSCF approach relative to the SCF HSE03-1/3x DF case.

This has resulted in a minor decrease in the slope of the reaction probability curve and, conversely, a slight increase in its width.

Irrespective of the small quantitative disagreement of sticking probabilities and barrier heights obtained with the NSCF and SCF approaches, the argument that originally inspired us to explore the NSCF approach (accurate while much cheaper computationally) still holds considerable credence based on the results of this chapter. It is clear that based on only a GGA density we can achieve a vast improvement of the interaction energy of  $O_2 + Al(111)$  simply by non-self-consistently applying a screened hybrid functional to a GGA electron density once. Based on the small differences between the SCF and the NSCF results, we conclude that the greater part of the error in describing the  $O_2 + Al(111)$  system with a GGA DF is functional-driven and not density-driven. However, the remaining disagreement between the SCF and NSCF results suggests that a small density-driven error from using a GGA-level functional is still present.

Increasing the width of the sticking curve of  $O_2$  on Al(111) remains a priority for future work as the onset of the sticking curve is described with good agreement with both the SCF and NSCF functionals. Previous work suggested that this could be achieved by increasing the corrugation and anisotropy of barriers by incorporating Van der Waals correlation into the DF. The QCT and hole model reaction probability comparison suggests that the corrugation and anisotropy of the barrier may, however, not be the only factors influencing the width of the sticking curve. Nonetheless, the effect of including Van der Waals correlation in the DF on the dynamics should still be investigated. At the same time, due to the low charge transfer energy, electron-hole-pair excitations may need to be taken into account in future work, which could help to further broaden the sticking curve. Furthermore, introducing surface atom motion could also affect the width of the computed sticking probability curve for  $O_2$  on Al(111) by either influencing the barriers via thermal surface atom displacements or through energy transfer between the motions of  $O_2$  and the Al surface atoms.

## 3.5 Appendices

This chapter has two minor appendices. The first (Section 3.5.1) compares the barrier energies extracted from the CRP-PES to the corresponding HSE03-1/3x@RPBE DFT energy and shows the difference in energy and the RMSE. The second appendix (Section 3.5.2) shows two figures presenting the different energy shifts between the QCT and hole model sticking probabilities.

## 3.5.1 CRP test set

**Table 3.3:** Barrier energies as extracted from the CRP PES, and computed with DFT single point calculations for the CRP barrier geometries, the deviation ( $\Delta$ ) between them, and the resulting root mean squared error based on the deviations. See **Figure 3.1B** for the name and location of the high symmetry sites; the  $O_2$  orientation is indicated with P(parallel) for  $\theta$ =90°, N(Normal) for  $\theta$ =0°, and T(Tilted) for  $\theta$ =45°.

Top N         29.833         29.735         -0.098           Top P, $\varphi$ : 0°         24.423         24.152         -0.271           Top P, $\varphi$ : 30°         24.409         24.189         -0.220           Bridge N         25.451         25.334         -0.117           Bridge P, $\varphi$ : 0°         6.559         6.533         -0.027           Bridge P, $\varphi$ : 60°         29.727         29.470         -0.257           Bridge P, $\varphi$ : 90°         51.360         54.332         2.972           TtF N         29.108         29.127         0.019           TtF T, $\varphi$ : 150°         37.979         37.285         -0.694           TtF T, $\varphi$ : 330°         16.625         16.686         -0.003           TtF T, $\varphi$ : 330°         16.625         16.625         0.000           TtF P, $\varphi$ : 240°         28.736         28.527         -0.209           TtH T, $\varphi$ : 330°         16.821         16.632         0.011           TtH T, $\varphi$ : 30°         16.821         16.832         0.011           TtH T, $\varphi$ : 120°         36.335         35.837         -0.498           TtH P, $\varphi$ : 210°         37.847         37.466         -0.381           FCC N         38.521         38.982	High Symmetry geometry	CRP HSE03-1/3x@RPBE Barrier height ( <i>kJ/mol</i> )	DFT HSE03-1/3x@RPBE Barrier height ( <i>k]/mol</i> )	Δ (DFT-CRP) Barrier height ( <i>k]/mol</i> )
Top P, $\varphi$ : $30^{\circ}$ $24.409$ $24.189$ $-0.220$ Bridge N $25.451$ $25.334$ $-0.117$ Bridge P, $\varphi$ : $0^{\circ}$ $6.559$ $6.533$ $-0.027$ Bridge P, $\varphi$ : $60^{\circ}$ $29.727$ $29.470$ $-0.257$ Bridge P, $\varphi$ : $90^{\circ}$ $51.360$ $54.332$ $2.972$ TtF N $29.108$ $29.127$ $0.019$ TtF T, $\varphi$ : $150^{\circ}$ $37.979$ $37.285$ $-0.694$ TtF T, $\varphi$ : $240^{\circ}$ $16.688$ $16.686$ $-0.003$ TtF P, $\varphi$ : $330^{\circ}$ $16.625$ $16.625$ $0.000$ TtF P, $\varphi$ : $330^{\circ}$ $12.835$ $12.624$ $-0.212$ TtH N $27.718$ $27.690$ $-0.028$ TtH T, $\varphi$ : $120^{\circ}$ $16.821$ $16.832$ $0.011$ TtH T, $\varphi$ : $210^{\circ}$ $36.335$ $35.837$ $-0.498$ TtH P, $\varphi$ : $120^{\circ}$ $36.335$ $35.837$ $-0.498$ TtH P, $\varphi$ : $120^{\circ}$ $37.466$ $-0.381$ FCC N, $\varphi$ : $330^{\circ}$ $32.487$		29.833	29.735	-0.098
Bridge N $25.451$ $25.334$ $-0.117$ Bridge P, $\varphi$ : 0° $6.559$ $6.533$ $-0.027$ Bridge P, $\varphi$ : 60° $29.727$ $29.470$ $-0.257$ Bridge P, $\varphi$ : 90° $51.360$ $54.332$ $2.972$ TtF N $29.108$ $29.127$ $0.019$ TtF T, $\varphi$ : $150^\circ$ $37.979$ $37.285$ $-0.694$ TtF T, $\varphi$ : $240^\circ$ $16.688$ $16.686$ $-0.003$ TtF T, $\varphi$ : $330^\circ$ $16.625$ $16.625$ $0.000$ TtF P, $\varphi$ : $240^\circ$ $28.736$ $28.527$ $-0.209$ TtF P, $\varphi$ : $330^\circ$ $12.835$ $12.624$ $-0.212$ TtH N $27.718$ $27.690$ $-0.028$ TtH T, $\varphi$ : $30^\circ$ $16.821$ $16.832$ $0.011$ TtH T, $\varphi$ : $210^\circ$ $36.335$ $35.837$ $-0.498$ TtH P, $\varphi$ : $30^\circ$ $12.313$ $12.031$ $-0.282$ TtH P, $\varphi$ : $120^\circ$ $37.847$ $37.466$ $-0.381$ FCC N $38.521$ $38.982$	Top P, φ: 0°	24.423	24.152	-0.271
Bridge $P, \varphi: 0^{\circ}$ $6.559$ $6.533$ $-0.027$ Bridge $P, \varphi: 60^{\circ}$ $29.727$ $29.470$ $-0.257$ Bridge $P, \varphi: 90^{\circ}$ $51.360$ $54.332$ $2.972$ TtF $N$ $29.108$ $29.127$ $0.019$ TtF $T, \varphi: 150^{\circ}$ $37.979$ $37.285$ $-0.694$ TtF $T, \varphi: 240^{\circ}$ $16.688$ $16.686$ $-0.003$ TtF $P, \varphi: 330^{\circ}$ $16.625$ $16.625$ $0.000$ TtF $P, \varphi: 330^{\circ}$ $12.835$ $12.624$ $-0.212$ TtH $N$ $27.718$ $27.690$ $-0.028$ TtH $T, \varphi: 30^{\circ}$ $16.821$ $16.832$ $0.011$ TtH $T, \varphi: 120^{\circ}$ $16.920$ $16.930$ $0.009$ TtH $P, \varphi: 210^{\circ}$ $36.335$ $35.837$ $-0.498$ TtH $P, \varphi: 30^{\circ}$ $12.313$ $12.031$ $-0.282$ TtH $P, \varphi: 120^{\circ}$ $37.847$ $37.466$ $-0.381$ FCC $N$ $38.521$ $38.982$ $0.460$ FCC $P, \varphi: 330^{\circ}$ $59.569$ $-0.457$ FCC $P, \varphi: 0^{\circ}$ $13.507$ $13.21$	Top P, φ: 30°	24.409	24.189	-0.220
Bridge $P, \varphi: 60^{\circ}$ $29.727$ $29.470$ $-0.257$ Bridge $P, \varphi: 90^{\circ}$ $51.360$ $54.332$ $2.972$ $TtF N$ $29.108$ $29.127$ $0.019$ $TtF T, \varphi: 150^{\circ}$ $37.979$ $37.285$ $-0.694$ $TtF T, \varphi: 240^{\circ}$ $16.688$ $16.686$ $-0.003$ $TtF T, \varphi: 330^{\circ}$ $16.625$ $16.625$ $0.000$ $TtF P, \varphi: 340^{\circ}$ $28.736$ $28.527$ $-0.209$ $TtF P, \varphi: 330^{\circ}$ $12.835$ $12.624$ $-0.212$ $TtH N$ $27.718$ $27.690$ $-0.028$ $TtH T, \varphi: 30^{\circ}$ $16.821$ $16.832$ $0.011$ $TtH T, \varphi: 120^{\circ}$ $16.920$ $16.930$ $0.009$ $TtH P, \varphi: 30^{\circ}$ $12.313$ $12.031$ $-0.282$ $TtH P, \varphi: 30^{\circ}$ $12.313$ $12.031$ $-0.282$ $TtH P, \varphi: 120^{\circ}$ $37.847$ $37.466$ $-0.381$ $FCC N$ $38.521$ $38.982$ $0.460$ $FCC T, \varphi: 330^{\circ}$ $60.026$ $59.569$ $-0.457$ $FCC P, \varphi: 0^{\circ}$ $13.50$	Bridge N	25.451	25.334	-0.117
Bridge $P, \varphi: 90^\circ$ $51.360$ $54.332$ $2.972$ $TtF N$ $29.108$ $29.127$ $0.019$ $TtF T, \varphi: 150^\circ$ $37.979$ $37.285$ $-0.694$ $TtF T, \varphi: 240^\circ$ $16.688$ $16.686$ $-0.003$ $TtF T, \varphi: 330^\circ$ $16.625$ $16.625$ $0.000$ $TtF P, \varphi: 240^\circ$ $28.736$ $28.527$ $-0.209$ $TtF P, \varphi: 330^\circ$ $12.835$ $12.624$ $-0.209$ $TtH N$ $27.718$ $27.690$ $-0.028$ $TtH T, \varphi: 30^\circ$ $16.821$ $16.832$ $0.011$ $TtH T, \varphi: 120^\circ$ $36.335$ $35.837$ $-0.498$ $TtH T, \varphi: 210^\circ$ $36.335$ $35.837$ $-0.498$ $TtH P, \varphi: 30^\circ$ $12.313$ $12.031$ $-0.282$ $TtH P, \varphi: 120^\circ$ $37.847$ $37.466$ $-0.381$ $FCC N$ $38.521$ $38.982$ $0.460$ $FCC T, \varphi: 150^\circ$ $32.487$ $32.623$ $0.136$ $FCC P, \varphi: 0^\circ$ $13.507$ $13.218$	Bridge P, φ: 0°	6.559	6.533	-0.027
$TtFN$ $29.108$ $29.127$ $0.019$ $TtFT, \varphi: 150^{\circ}$ $37.979$ $37.285$ $-0.694$ $TtFT, \varphi: 240^{\circ}$ $16.688$ $16.686$ $-0.003$ $TtFT, \varphi: 330^{\circ}$ $16.625$ $16.625$ $0.000$ $TtFP, \varphi: 240^{\circ}$ $28.736$ $28.527$ $-0.209$ $TtFP, \varphi: 330^{\circ}$ $12.835$ $12.624$ $-0.212$ $TtHN$ $27.718$ $27.690$ $-0.028$ $TtHT, \varphi: 30^{\circ}$ $16.821$ $16.832$ $0.011$ $TtHT, \varphi: 120^{\circ}$ $16.920$ $16.930$ $0.009$ $TtHT, \varphi: 210^{\circ}$ $36.335$ $35.837$ $-0.498$ $TtHP, \varphi: 30^{\circ}$ $12.313$ $12.031$ $-0.282$ $TtHP, \varphi: 120^{\circ}$ $37.847$ $37.466$ $-0.381$ $FCCN$ $38.521$ $38.982$ $0.460$ $FCCT, \varphi: 150^{\circ}$ $32.487$ $32.623$ $0.136$ $FCCT, \varphi: 330^{\circ}$ $60.026$ $59.569$ $-0.457$ $FCCP, \varphi: 330^{\circ}$ $14.612$ $14.289$ $-0.289$ $FCCP, \varphi: 300^{\circ}$ $34.616$	Bridge P, φ: 60°	29.727	29.470	-0.257
$TtFT, \varphi: 150^{\circ}$ $37.979$ $37.285$ $-0.694$ $TtFT, \varphi: 240^{\circ}$ $16.688$ $16.686$ $-0.003$ $TtFT, \varphi: 330^{\circ}$ $16.625$ $0.000$ $TtFP, \varphi: 240^{\circ}$ $28.736$ $28.527$ $-0.209$ $TtFP, \varphi: 330^{\circ}$ $12.835$ $12.624$ $-0.212$ $TtHN$ $27.718$ $27.690$ $-0.028$ $TtHT, \varphi: 30^{\circ}$ $16.821$ $16.832$ $0.011$ $TtHT, \varphi: 120^{\circ}$ $16.920$ $16.930$ $0.009$ $TtHP, \varphi: 30^{\circ}$ $12.313$ $12.031$ $-0.282$ $TtHP, \varphi: 30^{\circ}$ $12.313$ $12.031$ $-0.282$ $TtHP, \varphi: 120^{\circ}$ $37.847$ $37.466$ $-0.381$ $FCCN$ $38.521$ $38.982$ $0.460$ $FCCT, \varphi: 150^{\circ}$ $32.487$ $32.623$ $0.136$ $FCCP, \varphi: 0^{\circ}$ $13.507$ $13.218$ $-0.289$ $FCCP, \varphi: 330^{\circ}$ $14.612$ $14.289$ $-0.332$ $HCPN$ $34.616$ $34.929$ $0.313$ $HCPT, \varphi: 30^{\circ}$ $56.217$ $56.139$ $-0.$	Bridge P, φ: 90°	51.360	54.332	2.972
$TtFT, \varphi: 240^\circ$ $16.688$ $16.625$ $16.625$ $0.000$ $TtFT, \varphi: 330^\circ$ $16.625$ $16.625$ $0.000$ $TtFP, \varphi: 240^\circ$ $28.736$ $28.527$ $-0.209$ $TtFP, \varphi: 330^\circ$ $12.835$ $12.624$ $-0.212$ $TtHN$ $27.718$ $27.690$ $-0.028$ $TtHT, \varphi: 30^\circ$ $16.821$ $16.832$ $0.011$ $TtHT, \varphi: 120^\circ$ $16.920$ $16.930$ $0.009$ $TtHT, \varphi: 210^\circ$ $36.335$ $35.837$ $-0.498$ $TtHP, \varphi: 30^\circ$ $12.313$ $12.031$ $-0.282$ $TtHP, \varphi: 120^\circ$ $37.847$ $37.466$ $-0.381$ $FCCN$ $38.521$ $38.982$ $0.460$ $FCCT, \varphi: 150^\circ$ $32.487$ $32.623$ $0.136$ $FCCT, \varphi: 330^\circ$ $60.026$ $59.569$ $-0.457$ $FCCP, \varphi: 0^\circ$ $13.507$ $13.218$ $-0.289$ $FCCP, \varphi: 330^\circ$ $14.612$ $14.289$ $-0.332$ $HCPT, \varphi: 210^\circ$ $30.969$ $31.125$ $0.156$ $HCPT, \varphi: 30^\circ$ $12.707$ <t< td=""><td>TtF N</td><td>29.108</td><td>29.127</td><td>0.019</td></t<>	TtF N	29.108	29.127	0.019
$TtF T, \varphi: 330^{\circ}$ $16.625$ $16.625$ $0.000$ $TtF P, \varphi: 240^{\circ}$ $28.736$ $28.527$ $-0.209$ $TtF P, \varphi: 330^{\circ}$ $12.835$ $12.624$ $-0.212$ $TtH N$ $27.718$ $27.690$ $-0.028$ $TtH T, \varphi: 30^{\circ}$ $16.821$ $16.832$ $0.011$ $TtH T, \varphi: 120^{\circ}$ $16.920$ $16.930$ $0.009$ $TtH P, \varphi: 30^{\circ}$ $12.313$ $12.031$ $-0.282$ $TtH P, \varphi: 120^{\circ}$ $37.847$ $37.466$ $-0.381$ $FCC N$ $38.521$ $38.982$ $0.460$ $FCC T, \varphi: 150^{\circ}$ $32.487$ $32.623$ $0.136$ $FCC T, \varphi: 330^{\circ}$ $60.026$ $59.569$ $-0.457$ $FCC P, \varphi: 0^{\circ}$ $13.507$ $13.218$ $-0.289$ $FCC P, \varphi: 330^{\circ}$ $14.612$ $14.289$ $-0.332$ $HCP N$ $34.616$ $34.929$ $0.313$ $HCP T, \varphi: 30^{\circ}$ $56.217$ $56.139$ $-0.078$ $HCP P, \varphi: 30^{\circ}$ $12.707$ $12.455$ $-0.252$ $HCP P, \varphi: 30^{\circ}$ $13.700$ <td>TtF Τ, φ: 150°</td> <td>37.979</td> <td>37.285</td> <td>-0.694</td>	TtF Τ, φ: 150°	37.979	37.285	-0.694
$TtF P, \varphi: 240^{\circ}$ $28.736$ $28.527$ $-0.209$ $TtF P, \varphi: 330^{\circ}$ $12.835$ $12.624$ $-0.212$ $TtH N$ $27.718$ $27.690$ $-0.028$ $TtH T, \varphi: 30^{\circ}$ $16.821$ $16.832$ $0.011$ $TtH T, \varphi: 120^{\circ}$ $16.920$ $16.930$ $0.009$ $TtH T, \varphi: 210^{\circ}$ $36.335$ $35.837$ $-0.498$ $TtH P, \varphi: 30^{\circ}$ $12.313$ $12.031$ $-0.282$ $TtH P, \varphi: 120^{\circ}$ $37.847$ $37.466$ $-0.381$ $FCC N$ $38.521$ $38.982$ $0.460$ $FCC T, \varphi: 150^{\circ}$ $32.487$ $32.623$ $0.136$ $FCC T, \varphi: 330^{\circ}$ $60.026$ $59.569$ $-0.457$ $FCC P, \varphi: 30^{\circ}$ $13.507$ $13.218$ $-0.289$ $FCC P, \varphi: 330^{\circ}$ $14.612$ $14.289$ $-0.332$ $HCP N$ $34.616$ $34.929$ $0.313$ $HCP T, \varphi: 210^{\circ}$ $30.969$ $31.125$ $0.156$ $HCP P, \varphi: 30^{\circ}$ $12.707$ $12.455$ $-0.252$ $HCP P, \varphi: 30^{\circ}$ $13.700$ </td <td>TtF Τ, φ: 240°</td> <td>16.688</td> <td>16.686</td> <td>-0.003</td>	TtF Τ, φ: 240°	16.688	16.686	-0.003
$TtF P, \varphi: 330^{\circ}$ $12.835$ $12.624$ $-0.212$ $TtH N$ $27.718$ $27.690$ $-0.028$ $TtH T, \varphi: 30^{\circ}$ $16.821$ $16.832$ $0.011$ $TtH T, \varphi: 120^{\circ}$ $16.920$ $16.930$ $0.009$ $TtH T, \varphi: 210^{\circ}$ $36.335$ $35.837$ $-0.498$ $TtH P, \varphi: 30^{\circ}$ $12.313$ $12.031$ $-0.282$ $TtH P, \varphi: 120^{\circ}$ $37.847$ $37.466$ $-0.381$ $FCC N$ $38.521$ $38.982$ $0.460$ $FCC T, \varphi: 150^{\circ}$ $32.487$ $32.623$ $0.136$ $FCC T, \varphi: 330^{\circ}$ $60.026$ $59.569$ $-0.457$ $FCC P, \varphi: 0^{\circ}$ $13.507$ $13.218$ $-0.289$ $FCC P, \varphi: 30^{\circ}$ $14.612$ $14.289$ $-0.332$ $HCP N$ $34.616$ $34.929$ $0.313$ $HCP T, \varphi: 210^{\circ}$ $30.969$ $31.125$ $0.156$ $HCP P, \varphi: 30^{\circ}$ $12.707$ $12.455$ $-0.252$ $HCP P, \varphi: 30^{\circ}$ $13.700$ $13.551$ $-0.149$	TtF Τ, φ: 330°	16.625	16.625	0.000
$TtH N$ $27.718$ $27.690$ $-0.028$ $TtH T, \varphi: 30^{\circ}$ $16.821$ $16.832$ $0.011$ $TtH T, \varphi: 120^{\circ}$ $16.920$ $16.930$ $0.009$ $TtH T, \varphi: 210^{\circ}$ $36.335$ $35.837$ $-0.498$ $TtH P, \varphi: 30^{\circ}$ $12.313$ $12.031$ $-0.282$ $TtH P, \varphi: 120^{\circ}$ $37.847$ $37.466$ $-0.381$ FCC N $38.521$ $38.982$ $0.460$ FCC T, $\varphi: 150^{\circ}$ $32.487$ $32.623$ $0.136$ FCC T, $\varphi: 330^{\circ}$ $60.026$ $59.569$ $-0.457$ FCC P, $\varphi: 0^{\circ}$ $13.507$ $13.218$ $-0.289$ FCC P, $\varphi: 330^{\circ}$ $14.612$ $14.289$ $-0.332$ HCP N $34.616$ $34.929$ $0.313$ HCP T, $\varphi: 210^{\circ}$ $30.969$ $31.125$ $0.156$ HCP T, $\varphi: 30^{\circ}$ $56.217$ $56.139$ $-0.078$ HCP P, $\varphi: 30^{\circ}$ $12.707$ $12.455$ $-0.252$ HCP P, $\varphi: 30^{\circ}$ $13.700$ $13.551$ $-0.149$	TtF P, φ: 240°	28.736	28.527	-0.209
$TtH T, \varphi: 30^{\circ}$ $16.821$ $16.832$ $0.011$ $TtH T, \varphi: 120^{\circ}$ $16.920$ $16.930$ $0.009$ $TtH T, \varphi: 210^{\circ}$ $36.335$ $35.837$ $-0.498$ $TtH P, \varphi: 30^{\circ}$ $12.313$ $12.031$ $-0.282$ $TtH P, \varphi: 120^{\circ}$ $37.847$ $37.466$ $-0.381$ $FCC N$ $38.521$ $38.982$ $0.460$ $FCC T, \varphi: 150^{\circ}$ $32.487$ $32.623$ $0.136$ $FCC T, \varphi: 330^{\circ}$ $60.026$ $59.569$ $-0.457$ $FCC P, \varphi: 30^{\circ}$ $13.507$ $13.218$ $-0.289$ $FCC P, \varphi: 30^{\circ}$ $14.612$ $14.289$ $-0.332$ $HCP N$ $34.616$ $34.929$ $0.313$ $HCP T, \varphi: 210^{\circ}$ $30.969$ $31.125$ $0.156$ $HCP T, \varphi: 30^{\circ}$ $56.217$ $56.139$ $-0.078$ $HCP P, \varphi: 0^{\circ}$ $12.707$ $12.455$ $-0.252$ $HCP P, \varphi: 30^{\circ}$ $13.700$ $13.551$ $-0.149$	TtF P, φ: 330°	12.835	12.624	-0.212
$TtH T, \varphi: 120^{\circ}$ $16.920$ $16.930$ $0.009$ $TtH T, \varphi: 210^{\circ}$ $36.335$ $35.837$ $-0.498$ $TtH P, \varphi: 30^{\circ}$ $12.313$ $12.031$ $-0.282$ $TtH P, \varphi: 120^{\circ}$ $37.847$ $37.466$ $-0.381$ $FCC N$ $38.521$ $38.982$ $0.460$ $FCC T, \varphi: 150^{\circ}$ $32.487$ $32.623$ $0.136$ $FCC T, \varphi: 330^{\circ}$ $60.026$ $59.569$ $-0.457$ $FCC P, \varphi: 0^{\circ}$ $13.507$ $13.218$ $-0.289$ $FCC P, \varphi: 30^{\circ}$ $14.612$ $14.289$ $-0.332$ $HCP N$ $34.616$ $34.929$ $0.313$ $HCP T, \varphi: 210^{\circ}$ $30.969$ $31.125$ $0.156$ $HCP T, \varphi: 30^{\circ}$ $56.217$ $56.139$ $-0.078$ $HCP P, \varphi: 0^{\circ}$ $12.707$ $12.455$ $-0.252$ $HCP P, \varphi: 30^{\circ}$ $13.700$ $13.551$ $-0.149$	TtH N	27.718	27.690	-0.028
$TtH T, \varphi: 210^{\circ}$ $36.335$ $35.837$ $-0.498$ $TtH P, \varphi: 30^{\circ}$ $12.313$ $12.031$ $-0.282$ $TtH P, \varphi: 120^{\circ}$ $37.847$ $37.466$ $-0.381$ $FCC N$ $38.521$ $38.982$ $0.460$ $FCC T, \varphi: 150^{\circ}$ $32.487$ $32.623$ $0.136$ $FCC T, \varphi: 330^{\circ}$ $60.026$ $59.569$ $-0.457$ $FCC P, \varphi: 0^{\circ}$ $13.507$ $13.218$ $-0.289$ $FCC P, \varphi: 330^{\circ}$ $14.612$ $14.289$ $-0.332$ $HCP N$ $34.616$ $34.929$ $0.313$ $HCP T, \varphi: 210^{\circ}$ $30.969$ $31.125$ $0.156$ $HCP T, \varphi: 30^{\circ}$ $56.217$ $56.139$ $-0.078$ $HCP P, \varphi: 0^{\circ}$ $12.707$ $12.455$ $-0.252$ $HCP P, \varphi: 30^{\circ}$ $13.700$ $13.551$ $-0.149$	TtH T, φ: 30°	16.821	16.832	0.011
$TtH P, \varphi: 30^{\circ}$ $12.313$ $12.031$ $-0.282$ $TtH P, \varphi: 120^{\circ}$ $37.847$ $37.466$ $-0.381$ $FCC N$ $38.521$ $38.982$ $0.460$ $FCC T, \varphi: 150^{\circ}$ $32.487$ $32.623$ $0.136$ $FCC T, \varphi: 330^{\circ}$ $60.026$ $59.569$ $-0.457$ $FCC P, \varphi: 0^{\circ}$ $13.507$ $13.218$ $-0.289$ $FCC P, \varphi: 330^{\circ}$ $14.612$ $14.289$ $-0.332$ $HCP N$ $34.616$ $34.929$ $0.313$ $HCP T, \varphi: 210^{\circ}$ $30.969$ $31.125$ $0.156$ $HCP T, \varphi: 30^{\circ}$ $56.217$ $56.139$ $-0.078$ $HCP P, \varphi: 0^{\circ}$ $12.707$ $12.455$ $-0.252$ $HCP P, \varphi: 30^{\circ}$ $13.700$ $13.551$ $-0.149$	TtH T, φ: 120°	16.920	16.930	0.009
$TtH P, \varphi: 120^{\circ}$ $37.847$ $37.466$ $-0.381$ $FCC N$ $38.521$ $38.982$ $0.460$ $FCC T, \varphi: 150^{\circ}$ $32.487$ $32.623$ $0.136$ $FCC T, \varphi: 330^{\circ}$ $60.026$ $59.569$ $-0.457$ $FCC P, \varphi: 0^{\circ}$ $13.507$ $13.218$ $-0.289$ $FCC P, \varphi: 330^{\circ}$ $14.612$ $14.289$ $-0.332$ $HCP N$ $34.616$ $34.929$ $0.313$ $HCP T, \varphi: 210^{\circ}$ $30.969$ $31.125$ $0.156$ $HCP T, \varphi: 30^{\circ}$ $56.217$ $56.139$ $-0.078$ $HCP P, \varphi: 0^{\circ}$ $12.707$ $12.455$ $-0.252$ $HCP P, \varphi: 30^{\circ}$ $13.700$ $13.551$ $-0.149$	TtH T, φ: 210°	36.335	35.837	-0.498
FCC N $38.521$ $38.982$ $0.460$ FCC T, $\varphi$ : $150^\circ$ $32.487$ $32.623$ $0.136$ FCC T, $\varphi$ : $330^\circ$ $60.026$ $59.569$ $-0.457$ FCC P, $\varphi$ : $0^\circ$ $13.507$ $13.218$ $-0.289$ FCC P, $\varphi$ : $330^\circ$ $14.612$ $14.289$ $-0.332$ HCP N $34.616$ $34.929$ $0.313$ HCP T, $\varphi$ : $210^\circ$ $30.969$ $31.125$ $0.156$ HCP T, $\varphi$ : $30^\circ$ $56.217$ $56.139$ $-0.078$ HCP P, $\varphi$ : $0^\circ$ $12.707$ $12.455$ $-0.252$ HCP P, $\varphi$ : $30^\circ$ $13.700$ $13.551$ $-0.149$	TtH P, φ: 30°	12.313	12.031	-0.282
FCC T, φ: 150°       32.487       32.623       0.136         FCC T, φ: 330°       60.026       59.569       -0.457         FCC P, φ: 0°       13.507       13.218       -0.289         FCC P, φ: 330°       14.612       14.289       -0.332         HCP N       34.616       34.929       0.313         HCP T, φ: 210°       30.969       31.125       0.156         HCP T, φ: 30°       56.217       56.139       -0.078         HCP P, φ: 0°       12.707       12.455       -0.252         HCP P, φ: 30°       13.700       13.551       -0.149	TtH P, φ: 120°	37.847	37.466	-0.381
$FCC\ T, \varphi: 330^\circ$ $60.026$ $59.569$ $-0.457$ $FCC\ P, \varphi: 0^\circ$ $13.507$ $13.218$ $-0.289$ $FCC\ P, \varphi: 330^\circ$ $14.612$ $14.289$ $-0.332$ $HCP\ N$ $34.616$ $34.929$ $0.313$ $HCP\ T, \varphi: 210^\circ$ $30.969$ $31.125$ $0.156$ $HCP\ T, \varphi: 30^\circ$ $56.217$ $56.139$ $-0.078$ $HCP\ P, \varphi: 0^\circ$ $12.707$ $12.455$ $-0.252$ $HCP\ P, \varphi: 30^\circ$ $13.700$ $13.551$ $-0.149$	FCC N	38.521	38.982	0.460
FCC P, $\varphi$ : 0°       13.507       13.218       -0.289         FCC P, $\varphi$ : 330°       14.612       14.289       -0.332         HCP N       34.616       34.929       0.313         HCP T, $\varphi$ : 210°       30.969       31.125       0.156         HCP T, $\varphi$ : 30°       56.217       56.139       -0.078         HCP P, $\varphi$ : 0°       12.707       12.455       -0.252         HCP P, $\varphi$ : 30°       13.700       13.551       -0.149	FCC Τ, φ: 150°	32.487	32.623	0.136
FCC P, $\varphi$ : 330°       14.612       14.289       -0.332         HCP N       34.616       34.929       0.313         HCP T, $\varphi$ : 210°       30.969       31.125       0.156         HCP T, $\varphi$ : 30°       56.217       56.139       -0.078         HCP P, $\varphi$ : 0°       12.707       12.455       -0.252         HCP P, $\varphi$ : 30°       13.700       13.551       -0.149	FCC Τ, φ: 330°	60.026	59.569	-0.457
HCP N       34.616       34.929       0.313         HCP T, φ: 210°       30.969       31.125       0.156         HCP T, φ: 30°       56.217       56.139       -0.078         HCP P, φ: 0°       12.707       12.455       -0.252         HCP P, φ: 30°       13.700       13.551       -0.149	FCC P, φ: 0°	13.507	13.218	-0.289
HCP N       34.616       34.929       0.313         HCP T, φ: 210°       30.969       31.125       0.156         HCP T, φ: 30°       56.217       56.139       -0.078         HCP P, φ: 0°       12.707       12.455       -0.252         HCP P, φ: 30°       13.700       13.551       -0.149	FCC P, φ: 330°	14.612	14.289	-0.332
HCP T, φ: 30°       56.217       56.139       -0.078         HCP P, φ: 0°       12.707       12.455       -0.252         HCP P, φ: 30°       13.700       13.551       -0.149		34.616	34.929	0.313
HCP P, φ: 0°       12.707       12.455       -0.252         HCP P, φ: 30°       13.700       13.551       -0.149	HCP Τ, φ: 210°	30.969	31.125	0.156
HCP P, φ: 30° 13.700 13.551 -0.149	HCP Τ, φ: 30°	56.217	56.139	-0.078
	HCP P, φ: 0°	12.707	12.455	-0.252
RMSE - 0.614	HCP P, φ: 30°	13.700	13.551	-0.149
	RMSE	-	-	0.614

## 3.5.2 Hole model and QCT energy shifts

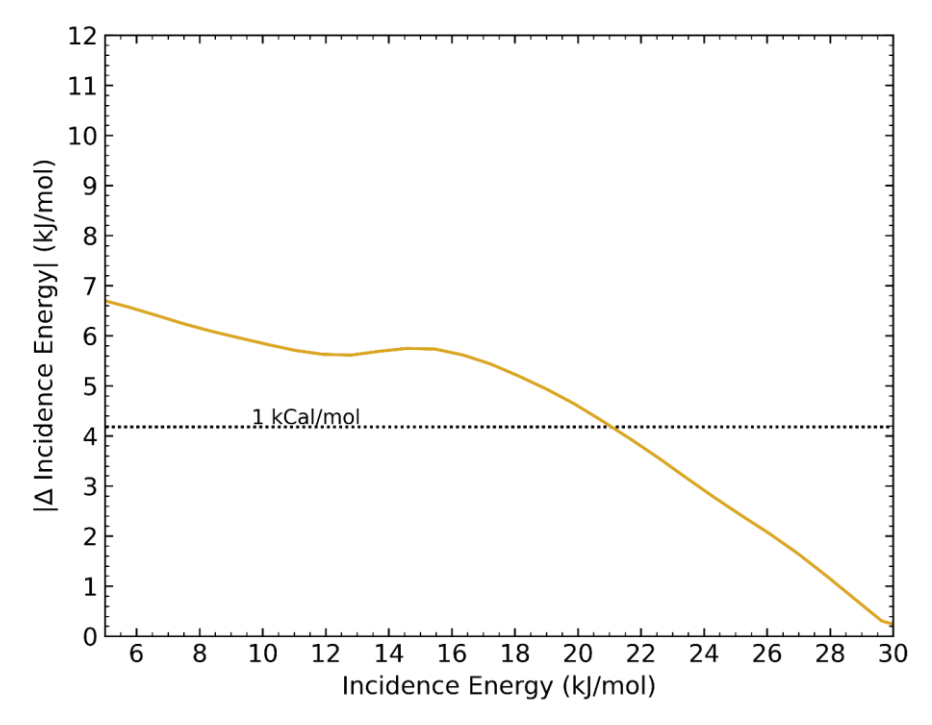


**Figure 3.9**: The absolute difference of incidence energy between the hole model reaction probability and the QCT reaction probability curve as a function of the incidence energy of the Hole model, moving the reaction probability curves in **Figure 3.8** from left (hole model) to right(QCT).

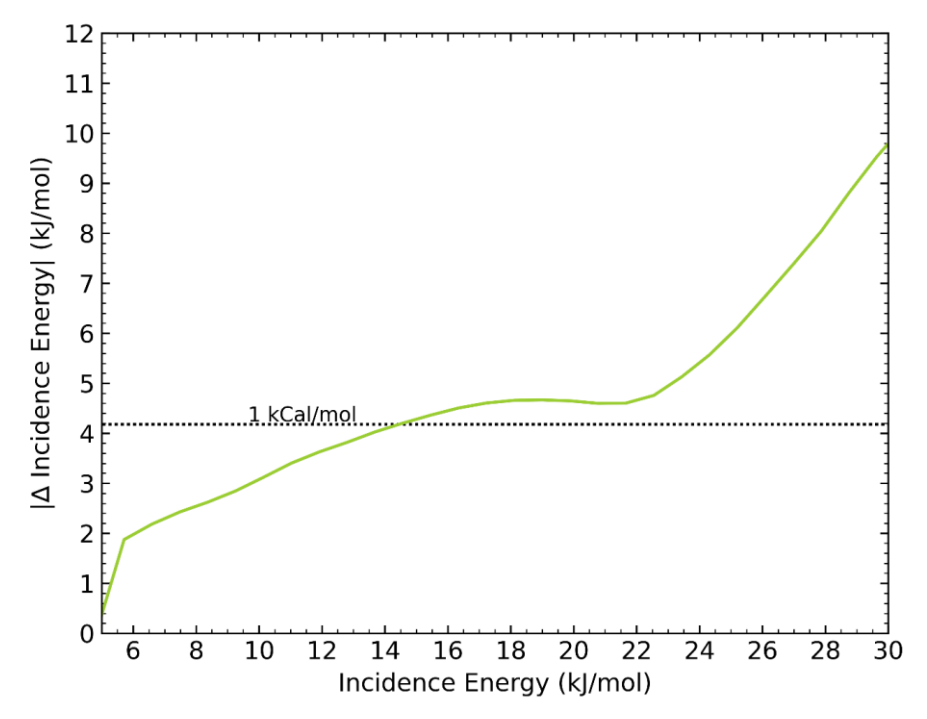


**Figure 3.10**: The absolute difference of incidence energy between the QCT reaction probability and the reaction probability curve of the hole model excluding vibrational energies as a function of the incidence energy of the QCT, moving the reaction probability curves in **Figure 3.8** from left(QCT) to right (hole model Excl. Vibrations).